Efficient microbial glucose-fructose conversion at ambient temperature through adaptive laboratory evolution and application for D-allulose production

Alexander Lehnert[1], Rocco Gentile[3], Claudia Tahiraj[1], Astrid Wirtz[1], Meike Baumgart[1], Tino Polen[1], Holger Gohlke[2,3,4], Michael Bott[1,4#]

[1]IBG-1: Biotechnology, Institute of Bio- and Geosciences, Forschungszentrum Jülich, Jülich, Germany

[2]IBG-4: Bioinformatics, Institute of Bio-and Geosciences, Forschungszentrum Jülich, Jülich, Germany

[3]Insitute for Pharmaceutical and Medicinal Chemistry, Heinrich-Heine-Universität Düsseldorf, Düsseldorf, Germany

[4]The Bioeconomy Science Center (BioSC), Forschungszentrum Jülich, Jülich, Germany

[#] Corresponding author: m.bott@fz-juelich.de

Graphical abstract

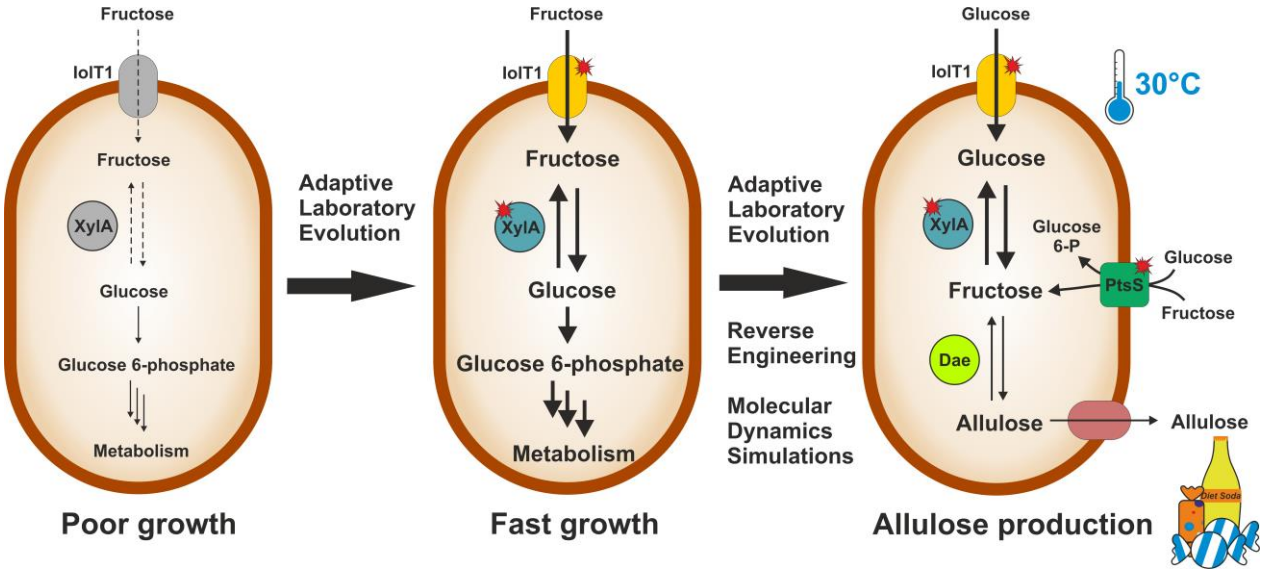

Abstract

Glucose and fructose, the major monosaccharides in nature, are metabolically interconverted in phosphorylated form by glucose 6-phosphate isomerase. An enzyme specifically evolved for interconversion of the non-phosphorylated forms has not been discovered yet. Xylose isomerase catalyzes the conversion as a side reaction, but with very low activity at ambient temperatures. Here, we developed a microbial catalyst enabling the efficient interconversion of glucose and fructose at 30°C. Using adaptive laboratory evolution (ALE) of a selection strain dependent on xylose isomerase activity for growth, we obtained enzyme variants with up to ten-fold improved catalytic efficiency. Fast growth additionally required a mutation in the transporter IolT1, boosting sugar uptake and increasing the intracellular substrate concentration. During engineering of a strain unable to grow on glucose, we identified mutations in the sucrose transporter PtsS, presumably converting it into a transporter for glucose and fructose. Molecular dynamics simulations of the transporter and xylose isomerase variants suggested mechanistic consequences of the mutations. Our novel strains enabled the microbial conversion of glucose to the low-calorie sweetener D-allulose with a yield of 15%.

Keywords: *Corynebacterium glutamicum*, adaptive laboratory evolution, directed evolution, sugar uptake, alternative sweetener, D-fructose, D-glucose, D-allulose

Introduction

Studies on the chemical isomerization of glucose to fructose were first performed by Cornelis Adriaan Lobry van Troostenburg de Bruyn and Willem Alberda van Ekenstein around 1895 [1]. As the base- or acid-catalyzed reversible transformation of an aldose into the ketose isomer involves a tautomeric enediol as reaction intermediate, also D-mannose is formed as product [2]. The first

enzymatic conversion of glucose to fructose was identified to be a side reaction of xylose isomerase (EC 5.3.1.5), which therefore is also termed glucose isomerase [3]. However, the K_m value for glucose is about two orders of magnitude higher than for xylose, indicating that xylose conversion to xylulose is the physiological function. Xylose isomerase is applied in the industrial production of high-fructose corn syrup (HFCS), a mixture of glucose and fructose that is used as a sweetener for beverages and processed foods [4-6]. Immobilized in fixed-bed reactors, xylose isomerase enables a fructose yield of 42% from a glucose feed stream at 60°C. To obtain HFCS with the preferred 55% fructose content, either chromatographic separation is required or a higher process temperature (>85°C), which shifts the thermodynamic equilibrium towards fructose [7]. For this purpose, enzymes with improved thermal stability obtained by protein engineering [8] or naturally thermostable enzymes from hyperthermophilic microorganisms are used [9,10].

Due to the huge market of HFCS of >9.2 billion tons/year [11], other applications of xylose isomerase for glucose isomerization are much smaller in scale. Commercially available xylose isomerase was used at 55°C to regenerate glucose from fructose in the production of kojibiose [12]. Xylose isomerase of *Acidothermus cellulolyticus* was coupled with lyxose isomerase for mannose production from glucose at 65°C [13]. In other applications, xylose isomerase was employed in combination with allulose 3-epimerase or tagatose 3-epimerase for the production of D-allulose from glucose or sucrose at 50°C [14,15]. D-Allulose, also named D-psicose, is a rare natural sugar that has gained strong interest as a dietary sweetener with a number of health benefits [16-18], and is generally recognized as safe by the FDA. It has 70% of the sweetness of sucrose, but its caloric content in humans is only <0.4 kcal/g compared to 4 kcal/g sucrose [19]. Industrial production of D-allulose is performed in enzyme reactors from fructose with allulose 3-epimerase or tagatose 3-epimerase or in combination with xylose isomerase from glucose [20]. The conversion of glucose to

allulose via fructose is performed at 50-60°C with immobilized enzymes. However, as the half-life of allulose 3-epimerases at these temperatures is quite low, reusability is limited [21].

The availability of a xylose isomerase with high activity for glucose isomerization at mesophilic temperatures would allow for lowering the reaction temperature and facilitate the development of a microbial production process avoiding the need for enzyme purification and immobilization. However, previous protein engineering studies on xylose isomerase for glucose isomerization focused on enzymes from thermophilic organisms, such as *Clostridium thermosulfurogenes* [22], *Thermus thermophilus* [23], or *Thermotoga neapolitana* [24] and used assay temperatures ≥60°C. In a directed evolution approach [25] with the *T. neapolitana* xylose isomerase, a microtiter plate assay was used to screen between 1000 and 1500 variants at 60°C and 80°C for improved properties [24].

In this study, we aimed to harness the power of *in vivo* selection to develop xylose isomerases efficiently catalyzing glucose isomerization within a microbial cell at 30°C. Such an approach has previously been used to increase the activity of xylose isomerization to xylulose in *Saccharomyces cerevisiae*, in order to improve bioethanol formation from xylose [26,27], but was not employed to improve the glucose isomerase activity of the enzyme at mesophilic temperatures. We developed a growth-based selection system with an engineered *Corynebacterium glutamicum* strain whose growth on fructose was dependent on its initial conversion to glucose by xylose isomerase. Adaptive laboratory evolution (ALE) [28,29] led to fast-growing strains whose analysis revealed the presence of xylose isomerase variants with an almost tenfold increased catalytic efficiency for fructose conversion to glucose, but additionally also fructose uptake into the cells was tenfold improved due to mutations in the sugar transporter. Combining the evolved proteins in a *C. glutamicum* strain unable to grow with glucose and equipped with allulose 3-epimerase allowed

the microbial conversion of glucose to allulose with similar yields as the process with immobilized enzymes.

Results

Design of a growth-based selection system for enhancing xylose isomerase activity for glucose-fructose interconversion

The major aim of our study was to find xylose isomerase variants that would enable the efficient microbial interconversion of glucose and fructose at mesophilic temperatures for subsequent application in production processes. Our approach was to exploit the power of ALE to select such enzymes. For this purpose, we initially created a bacterial selection strain whose growth on fructose was strictly dependent on the conversion to glucose by the activity of xylose isomerase. As a host we choose *Corynebacterium glutamicum*, used industrially for amino acid production in the million ton scale [30-33], because transport and metabolism of fructose and glucose are well known in this species with an optimal growth temperature of 30°C [34,35].

In *C. glutamicum*, fructose metabolization starts via the uptake of fructose as fructose 1-phosphate by the EII permease PtsF of the phosphoenolypyruvate-dependent phosphotransferase system (PTS). In a side reaction, also the EII permease for glucose, PtsG, can import fructose as fructose 6-phosphate [36,37]. In addition, also the secondary transporter IolT1, whose native substrates are inositols [38,39] and which is induced by these compounds via the transcriptional regulator IolR [40], is able to import fructose as well as glucose and xylose in their unphosphorylated forms [41-44]. However, since *C. glutamicum* lacks fructokinase activity, the imported fructose cannot be metabolized. Therefore, the deletion of PtsF and PtsG is sufficient to abolish the growth on fructose [45].

To construct a selection strain whose growth is dependent on glucose isomerase activity, we deleted *ptsF* and *ptsG* in the parental strain *C. glutamicum* MB001 [46]. To enable constitutive expression of *iolT1* for fructose uptake, one can delete the repressor IolR. However, as this causes induction of the entire IolR regulon [40], we specifically prevented IolR-mediated repression of *iolT1* by mutating the IolR-binding site in the promoter region, which abolished binding of IolR to its operator [41]. The resulting strain *C. glutamicum* Fru^{neg} showed negligible growth in fructose minimal medium, while growth in glucose minimal medium was only slightly reduced ($\mu = 0.34 \pm 0.02\ h^{-1}$) compared to strain MB001 ($\mu = 0.45 \pm 0.01\ h^{-1}$) (Fig. 1A, Fig. 1B). This difference is due to the absence of PtsG and uptake of glucose by IolT1.

We then performed literature search for xylose isomerases that might be suitable to enable at least minimal growth of strain Fru^{neg}. So far, only a few xylose isomerases were described to show activity for glucose at 30°C (Tab. S1), and the ones of *Arthrobacter* strain N.R.R.L B3728 ($XylA_{AB}$), *Anoxybacillus gonensis* ($XylA_{AG}$), *Escherichia coli* ($XylA_{EC}$), *Piromyces* sp. E2 ($XylA_{PE2}$), *Streptomyces murinus* ($XylA_{SM}$), *Paenibacillus* sp. R4 ($XylA_{PR4}$), and *Xanthomonas campestris* ($XylA_{XC}$) were selected for the construction of expression plasmids. $XylA_{XC}$ has not been characterized yet, but its gene was functionally expressed in *C. glutamicum* and enabled efficient xylose metabolization [47]. The selected *xylA* genes were cloned into the expression plasmid pPREx2 under the control of an IPTG-inducible *tac* promoter [48] and were transferred into strain Fru^{neg} (Fig. 1C). The recombinant strains were then tested for growth in fructose minimal medium (Fig. 1D). Compared to the residual growth of the control strain with pPREx2, all strains carrying one of the *xylA* expression plasmids grew slightly better. The best growth (Fig. 1D, Fig. 1E, Fig. S1A) and the highest fructose consumption (Fig. 1F) were observed with the xylose isomerases of *Arthrobacter* and *X. campestris*. This experiment confirmed that our selection strain was suitable for identifying XylA variants with improved glucose isomerase activity at 30°C.

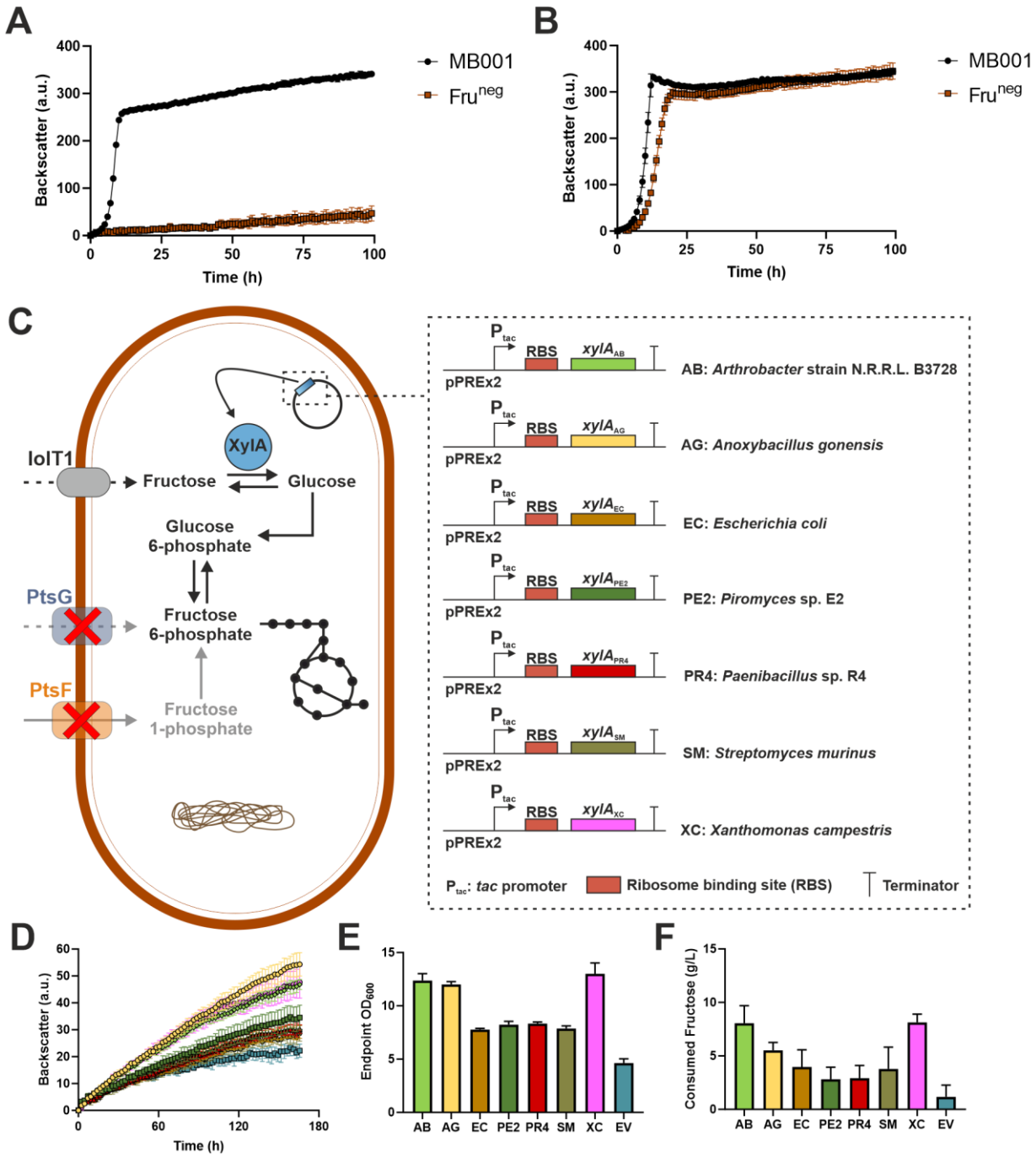

Fig 1. Growth performance of the fructose-negative strain Fru^{neg} in the absence and presence of *xylA* expression plasmids. The Fru^{neg} strain and its parental strain MB001 were cultivated in CGXII medium with 20 g/L fructose (A) or 20 g/L (w/v) glucose (B) at 30 °C and 1200 rpm for 100 h in a BioLector microcultivation system. (C) Scheme of the selection strain Fru^{neg} and the pPREx2-based *xylA* expression plasmids. (D) Growth of Fru^{neg} transformed with either one of the seven *xylA* expression plasmids or the vector control pPREx2 (EV) in CGXII medium with 40 g/L fructose, 25 µg/mL kanamycin and 1 mM IPTG. The cultures were inoculated to an initial OD_{600} of 7.5. (E) Final optical densities at 600 nm (OD_{600}) of the cultures shown in panel C after 160 h. (F) Fructose consumed by the cultures shown in panel C after 160 h. All data points given represent average values with standard deviations of three biological replicates.

Adaptive laboratory evolution of strain Fru^{neg} with *xylA* expression plasmids for improved growth on fructose

Although XylA$_{AB}$ and XylA$_{XC}$ allowed reasonable growth of the Fru^{neg} strain in fructose minimal medium, both strains barely doubled their initial OD_{600} and consumed less than 20 % of the fructose during 160 h cultivation (Fig. 1E, Fig. 1F). This suggested an intrinsically weak fructose-isomerizing activity for both xylose isomerases. To accelerate fructose metabolization and thus growth by improving XylA$_{AB}$ or XylA$_{XC}$ activity, ALE of strains Fru^{neg} pPREx2-*xylA*$_{AB}$ (AB) and Fru^{neg} pPREx2-*xylA*$_{XC}$ (XC) was performed in three biological replicates in 24-well plates (Fig. 2A). After 3-5 serial cultivations lasting for 5-15 days over a total period of 45-55 days in CGXII medium with 40 g/L fructose, 25 µg/mL kanamycin and 1 mM IPTG, the growth rate and the cell density of all six cultures were strongly increased. Then, aliquots of each culture were plated in a 1:100,000 dilution on CGXII agar plates with the same composition as the medium used for ALE (Fig. 2A). Small and large colonies appeared after 4-5 days of incubation at 30°C and one single large colony of each plate was picked and used for a growth experiment in the BioLector (Fig. 2A). All of the evolved strains (FAB evo 1-3, FXC evo 1-3) grew much faster and reached a much higher OD_{600} than the parental and control strains and consumed the entire fructose (Fig. 2B-2G, Fig. S1).

In order to elucidate the molecular basis for the improved growth of the evolved strains, their plasmid DNA was sequenced (Tab. 1). In the three independently evolved strains with the *Arthrobacter xylA* gene, two different mutations were identified in pPREx2-*xylA*$_{AB}$. Strain AB evo1 contained a Ser2Phe exchange in XylA, whereas strains AB evo2 and evo3 revealed a cytosine to thymine exchange 20 bp upstream of the *xylA*$_{AB}$ start codon (6 bp upstream of the RBS). The latter mutation might cause improved translation of the *xylA* mRNA leading to more XylA protein and higher enzyme activity. In the case of the S2F mutation, the effect might also be caused by

increased translation or by improving the catalytic activity of the enzyme for fructose isomerization to glucose. Remarkably, the three independently evolved strains with the *X. campestris xylA* gene all carried an identical mutation, a Trp147Ser exchange in the xylose isomerase, suggesting that this mutation stimulates fructose isomerization to glucose by the $XylA_{XC}$ enzyme. Besides the plasmid DNA, we also sequenced the genomic DNA of the six evolved strains. Remarkably, all contained only one mutation in the same gene, which was *iolT1* encoding the transporter for fructose uptake (Tab. 1). Strains FAB evo 1, FAB evo 3, FXC evo 1, and FXC evo 2 contained a Gly87Ser exchange in IolT1, whereas strains FAB evo 2 and FXC evo 3 harbored a Thr351Pro exchange in IolT1.

The sequencing results suggested that the combination of two effects was responsible for enabling improved growth on fructose, namely an improved fructose conversion to glucose by elevated levels of $XylA_{AB}$ or improved activity of $XylA_{XC}$ and an improved fructose uptake, possibly increasing the cytoplasmic fructose concentration and thereby XylA activity. To confirm the relevance of the individual mutations and the idea that the combination of *xylA* and *iolT1* mutations is required to achieve fast growth on fructose, we introduced the mutations singly or in combination into the parent strain Fru^{neg} carrying either pPREx2-$xylA_{AB}$ or pPREx2-$xylA_{XC}$. In total, the single mutations *iolT1*-T351P, *iolT1*-G87S, $xylA_{AB}$-S2F, $xylA_{AB}$_c_t, and $xylA_{XC}$-W147S and various combinations were tested for growth in fructose minimal medium and the results are shown in Figs. S2 and S3.

Table 1. Sequencing results of evolved Fru^{neg} pPREx2-*xylA* strains obtained via adaptive laboratory evolution for fast growth on fructose.

Strain	Location of mutation	Mutation
FAB evo 1	*xylA*$_{AB}$ (plasmid)	S2F
	iolT1 (genome)	G87S
FAB evo 2	pPREx2 (plasmid)	c to t mutation 20 bp upstream of *xylA*$_{AB}$ start codon (c_t)
	iolT1 (genome)	T351P
FAB evo 3	pPREx2 (plasmid)	c to t mutation 20 bp upstream of *xylA*$_{AB}$ start codon (c_t)
	iolT1 (genome)	G87S
FXC evo 1	*xylA*$_{XC}$ (plasmid)	W147S
	iolT1 (genome)	G87S
FXC evo 2	*xylA*$_{XC}$ (plasmid)	W147S
	iolT1 (genome)	G87S
FXC evo 3	*xylA*$_{XC}$ (plasmid)	W147S
	iolT1 (genome)	T351P

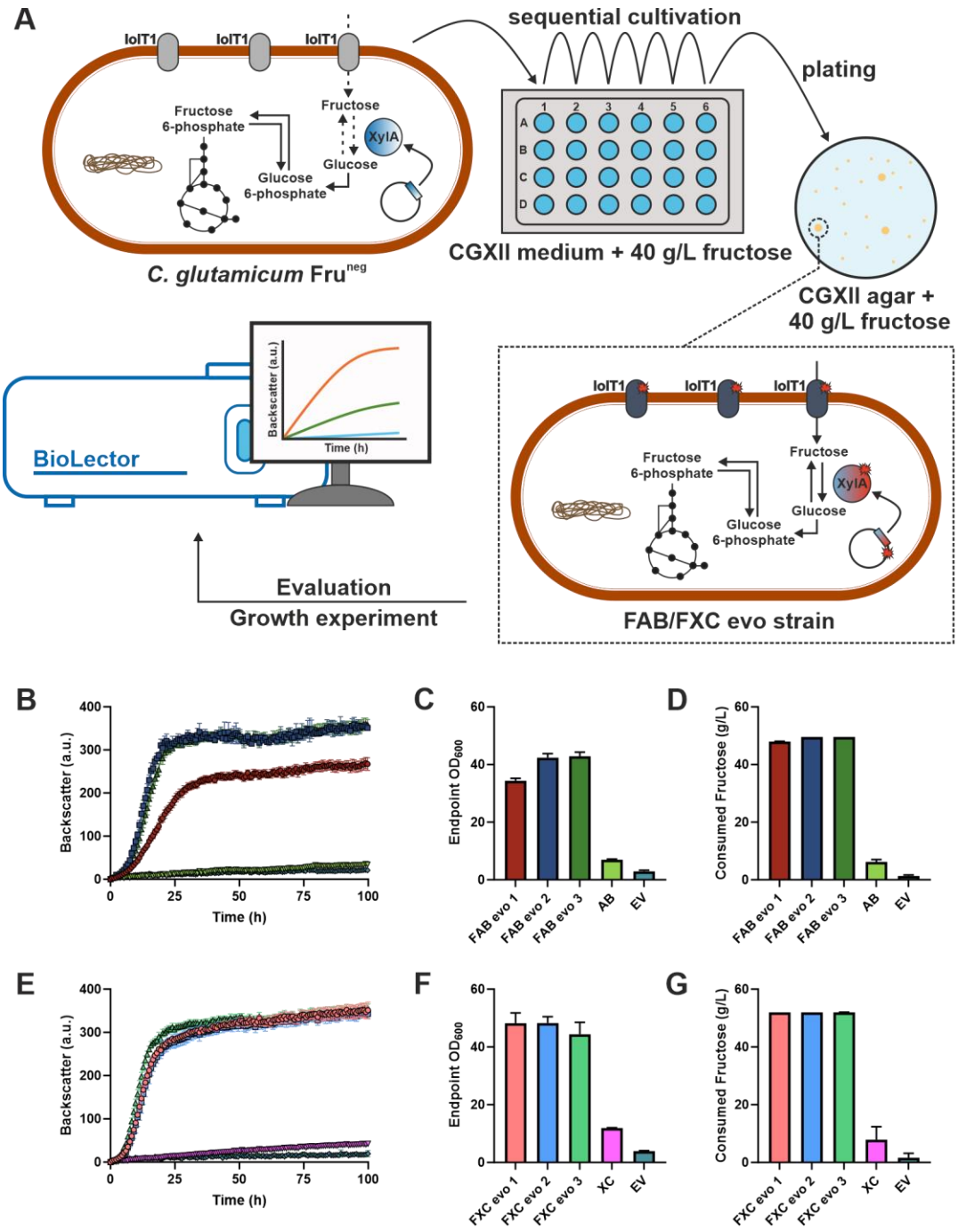

Fig. 2. Adaptive laboratory evolution (ALE) in fructose minimal medium of strain Fru^{neg} harboring either pPREx2-*xylA*$_{AB}$ or pPREx2-*xylA*$_{XC}$. (A) Design of the ALE. The cultivations were performed in CGXII medium with 40 g/L fructose, 25 µg/mL kanamycin and 1 mM IPTG in 24-well plates at 30 °C and 900 rpm for a duration of 5-15 days, after which an aliquot of each culture was used to inoculate fresh medium. In total, 2-4 transfers were made. After a duration of 45-55 days in total, the ALE was terminated and 100 µL of each culture was diluted by a factor of 100,000 and plated on CGXII agar plates with 40 g/L fructose to obtain single colonies. Comparatively large colonies were selected and used for a growth experiment in the same medium used for ALE (panels B-G). Each ALE was performed in biological triplicates. (B, C, D) BioLector II growth experiment of the selected evolved Fru^{neg} pPREx2-*xylA*$_{AB}$ strains (FAB evo 1-3) compared to the unevolved (AB) strain and the empty vector (EV) control. (E, F, G)

BioLector II growth experiment of evolved Fru^{neg} pPREx2-$xylA_{XC}$ (FXC evo 1-3) and unevolved (XC) strain as well as empty vector (EV) control. In panels B and E the backscatter values are shown, in panels C and F the final OD_{600} after 100 h, and in panels D and F the consumed fructose. Inoculation was performed to an initial OD_{600} of 5. All data points represent average values with standard deviations of three biological replicates.

Reconstruction of *iolT1* and pPREx2-*xylA* mutations in Fru^{neg} revealed that all introduced mutations showed a positive effect on growth, but the single mutations in *iolT1*, i.e. T351P and G87S, pushed growth and fructose consumption more strongly than the individual *xylA* mutations. However, the combination of *iolT1* and *xylA* mutations was necessary and sufficient to obtain strains with growth characteristics similar to the respective ALE-evolved strains containing the same mutations (Fig. S2, Fig. S3). While pPREx2-*xylA* related mutations increased the growth rate maximally twofold, the G87S or T351P mutations in *iolT1* enhanced the growth rate by three- to sevenfold.

In-depth analysis of IolT1 mutations via determination of K_s values and molecular dynamics simulations

Reconstruction of the evolved strains had demonstrated the importance of the G87S and T351P mutations in IolT1 to achieve fast growth of *xylA*-containing Fru^{neg} strains in fructose minimal medium. In order to characterize the effect of these mutations in more detail, we determined the growth rate at varying concentrations of fructose for the strain with wild-type IolT1, the two variants $IolT1^{G87S}$ and $IolT1^{T351P}$, and the double mutant $IolT1^{G87S\text{-}T351P}$. The substrate concentration at which a half-maximal growth rate is achieved represents the K_s value. For this experiment, the strains were transformed with the expression plasmid pPREx2-*scrK* that encodes the fructokinase gene *scrK* of *Clostridium acetobutylicum* and is active in *C. glutamicum* [43,49]. With this enzyme, fructose taken up by IolT1 is phosphorylated to fructose 6-phosphate enabling growth of the cells in fructose minimal medium [45] independent of xylose isomerase activity. Strain Fru^{neg}

pPREx2-*scrK* with wild-type IolT1 grew poorly in fructose minimal medium with a maximal growth rate (μ_{max}) of 0.032 ± 0.003 h^{-1} and a K_S value of 106.7 ± 7.8 mM (Fig. 3, Fig. S4, Tab. 2). Introduction of the single G87S or T351P and the double G87S-T351P amino acid exchanges enhanced the growth rate about 10-fold, resulting in μ_{max} values of 0.329 ± 0.017 h^{-1} or 0.336 ± 0.013 h^{-1} and 0.380 ± 0.003 h^{-1}, respectively, and K_S values of 80.2 ± 1.8 mM or 72.6 ± 4.2 mM and 93.3 ± 3.3 mM, respectively (Fig. 3, Fig. S4, Tab. 2). In general, these results confirm that both identified mutations in IolT1 strongly improve its ability for fructose transport. A combination of both mutations further improved μ_{max} by 13 % and 15 % but concomitantly increased the K_S value by 29 % and 16 % in contrast to T351P and G87S, respectively. Hence, the combination of both mutations did not increase fructose uptake over the impact caused by the single mutations.

Besides fructose, we also tested the growth rate dependency on the glucose concentration. In this case, no plasmid was required due to the availability of endogenous glucokinases in *C. glutamicum* that phosphorylate the imported glucose to glucose 6-phosphate [50,51]. Compared to fructose, strain Fru^{neg} with wild-type IolT1 reached an almost ten-time higher μ_{max} of 0.294 ± 0.01 h^{-1} and a six-time lower K_S value of 18.9 ± 2.8 mM (Fig. 3, Fig. S4, Tab. 2), suggesting a substrate preference for glucose over fructose by IolT1. Introduction of the G87S or T351P amino acid exchanges increased the growth rate to μ_{max} values of 0.548 ± 0.017 h^{-1} and 0.523 ± 0.004 h^{-1}, respectively, and decreased the K_S values to 1.9 ± 0.8 mM and 1.2 ± 1.0 mM, respectively (Fig. 3, Tab. 2). In contrast, introduction of the double mutant G87S-T351P resulted in a slightly decreased μ_{max} value of 0.519 ± 0.039 h^{-1} but strongly increased the K_S value to 4.9 ± 1.5 mM, compared to the single mutations, suggesting a rather detrimental effect on glucose transport.

In summary, the single mutations G87S and T351P improve fructose and glucose import by an order of magnitude regarding μ_{max} and K_S, respectively. The combination of both mutations in IolT1 does not exceed the kinetic parameters obtained for the single mutations, and, on the contrary,

results in a slightly and moderately negative effect on fructose and glucose import, respectively. How both mutations, and the combination of both mutations, act on a molecular level of the transport itself was investigated by performing molecular dynamic (MD) simulations.

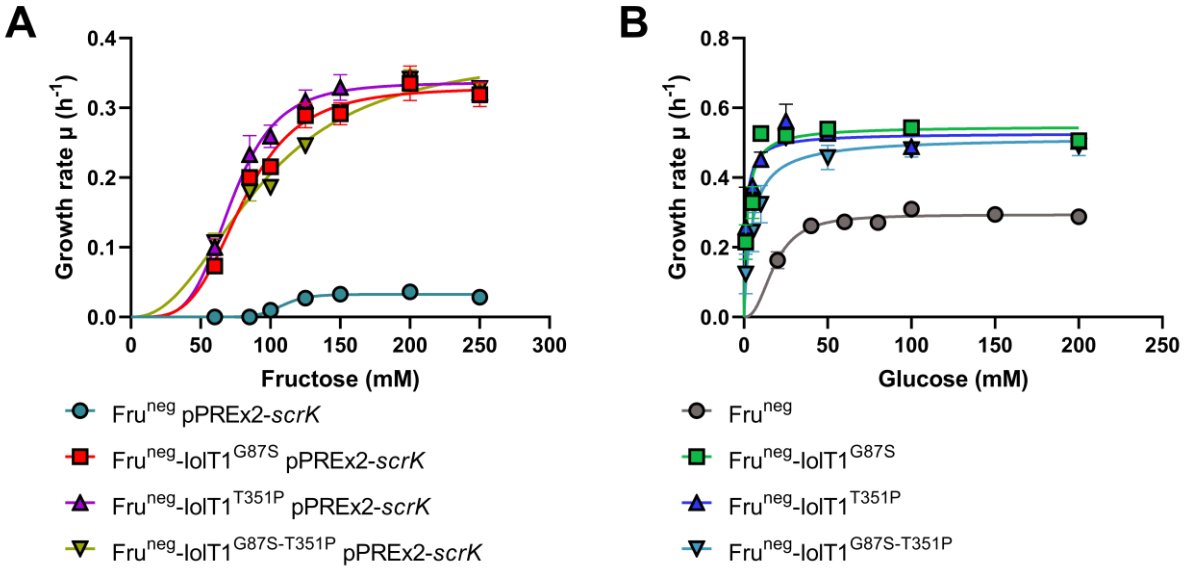

Fig. 3. Dependency of the growth rate from the concentrations of fructose (A) and glucose (B) in the medium for *C. glutamicum* Fru^{neg} containing either wild-type IolT1 or IolT1-G87S (Fru^{neg}-IolT1^{G87S}) or IolT1-T351P (Fru^{neg}-IolT1^{T351P}). Growth experiments in fructose minimal medium were performed with Fru^{neg} strains containing the pPREx2-*scrK* plasmid, expressing fructokinase from *C. acetobutylicum*. The minimal medium was additionally supplemented with 1 mM IPTG and 25 µg/mL kanamycin. Growth experiments in glucose minimal medium were performed with Fru^{neg} strains without a plasmid and minimal medium without IPTG and kanamycin. All experiments were conducted in a BioLector XT cultivation system at 30 °C and 1200 rpm for 24-48 h. Inoculation was performed to an initial OD_{600} of 5. All data points given represent average values with standard deviations of three biological replicates.

Table 2: Kinetic growth parameters for Fru^{neg} strains cultivated in CGXII medium with varying fructose or glucose concentrations.

Substrate	Strain	μ_{max} (h^{-1})	K_S (mM)
Fructose	Fru^{neg} pPREx2-*scrK*	0.032 ± 0.003	106.7 ± 7.8
	Fru^{neg}-IolT1^{G87S} pPREx2-*scrK*	0.329 ± 0.017	80.2 ± 1.8
	Fru^{neg}-IolT1^{T351P} pPREx2-*scrK*	0.336 ± 0.013	72.6 ± 4.2
	Fru^{neg}-IolT1$^{G87S-T351P}$ pPREx2-*scrK*	0.380 ± 0.003	93.3 ± 3.3
Glucose	Fru^{neg}	0.294 ± 0.010	18.9 ± 2.8
	Fru^{neg}-IolT1^{G87S}	0.548 ± 0.017	1.9 ± 0.8
	Fru^{neg}-IolT1^{T351P}	0.523 ± 0.004	1.2 ± 1.0
	Fru^{neg}-IolT1$^{G87S-T351P}$	0.519 ± 0.039	4.9 ± 1.5

To assess the influence of the G87S and T351P substitutions on the structural stability of IolT1, we performed all-atom unbiased MD simulations [52] of structural models of IolT1 in four different configurations, in part bound to glucose (as β-D-glucopyranose, BGP) and fructose (as β-D-fructofuranose, BFF), inserted into the lipid bilayer according to the OPM (Orientations of Proteins in Membranes) database (Fig. S5-11, Table S2) [53]. Starting structures of the variants were generated using the FoldX suite [54]. In all cases, the change in the folding free energy $\Delta\Delta G$ upon substitution is <3 kcal/mol, which indicates that the substitution is not considered destabilizing [55,56]. The membrane composition used was phosphatidylglycerol 16:0-18:1, cardiolipin 16:0-18.1, and phosphatidylinositol 16:0-18:1 in a ratio of 6:2:1, resembling the composition of the inner membrane of *C. glutamicum* [57,58]. For each configuration, five replicas were simulated, each for 500 ns in length. We used the generated conformations to probe if substitutions G87S, T351P, and G87S-T351P change the structural stability of IolT1 by applying a model of dynamic allostery [59-61] used on receptors and transporters before [62-64]. The model describes allosteric effects due to substitutions in terms of the per-residue (i, eq. 2) or per-region (r, eq. 3) rigidity index $\Delta r_{i/r,(Mutant-WT)}$ [61]. We evaluated $\Delta r_{i/r,(Mutant-WT)}$ for the helices 290-306 and 390-401, which are involved in the binding of the carbohydrate ligand in the outward-occluded and inward-occluded configurations and are critical for the carbohydrate transport to the inside of the cell, as found for the human GLUT

transporter [65]. There, the helices are named TM7b and TM10b. Conformational changes of these helices during the transport cycle are common in the major facilitator superfamily (MFS) [66] and accompany the rocker-switch mechanism used by MFS transporters.

The helices are more than 20 and 12 Å away from the substitutions G87S and T351P, respectively (Fig. 4A). The substitutions are not near other parts of the transport pathway either such that a trivial impact on the transport process is unlikely. The model of dynamic allostery reveals a configuration-, substitution type-, and carbohydrate-dependent impact on the structural stability of both helices. First, the substitutions destabilize the helices in the outward-open configuration, whereas they stabilize them in the inward-open configuration (Fig. 4A-B). In between, in the outward-occluded configuration, helix 290-306 becomes destabilized and helix 390-401 stabilized; in turn, in the inward-occluded configuration, helix 390-401 becomes destabilized and helix 290-306 stabilized. In either case, the destabilization or stabilization is less than in the outward-open or inward-open configurations, respectively. Second, these effects decrease in the order of the substitutions T351P > G87S > G87S-T351P, i.e., in correlation with the substitution effects on the growth rate (Fig. 3). Note that substitution effects on structural stability are not necessarily additive, which can explain why the impact of the double substitution is lower than that of the single ones [67]. Finally, the (de-)stabilizing effects for the two occluded states are generally weaker in the case of bound fructose than glucose (Fig. 4B), again in line with the difference in growth rates between the two carbohydrates (Fig. 3). Compared to wild-type IolT1, this leads to a succession of configurations with increasing structural stability along the transport cycle (Fig. 4B), which favors the inward-open configuration as the most structurally stable. These changes could result in the enhanced transport of the cargo from the outside to the inside of the cell.

While the gradient-driven transport is initiated by the binding of the cargo to the outward-open configuration [68], the reset of the transporter from the inward-open to the outward-open configuration is known for other carbohydrate transporters, such as the lactose permease in *E. coli* [69,70], to involve interactions of lipid head groups with charged amino acids to accommodate the energetic barrier imposed by salt bridges in the inward-open configuration. In IolT1, after the release of the carbohydrate on the intracellular side, D46 in TM1 and E400 in TM10b are thought to trigger the resetting between inward- and outward-facing conformations similarly to what has been suggested in other carbohydrate transporters [69,70]. MD simulations of IolT1 revealed that the PG lipid headgroups interact with D46 and E400, which form salt bridges to R126 (100.0% of total frames) and R339 (75.9% of total frames), respectively (Fig. S12, Fig. S13). The substitutions do not affect such salt bridges (Fig. S12, Fig. S13), thus, they should not influence the reset process.

To explain the difference in transport between glucose and fructose, we assessed the impact of helices 290-306 and 390-401 on carbohydrate binding in the outward-occluded and inward-occluded states by computing residue-wise binding effective energies. Glucose was found to bind stronger than fructose, in both the wild-type protein and the variants, and irrespective of the IolT1 configuration (Fig. 4C). A less favorable binding of fructose likely impacts the transport rate of the carbohydrate. The IolT1 variants revealed stronger interactions with the carbohydrates than wild-type IolT1, suggesting that allosteric effects due to the substitutions can improve the binding of the carbohydrates in addition to impacting the structural stability of the transporter (Fig. 4C). To conclude, substitutions T351P and G87S allosterically impact functionally relevant helices of IolT1, and the impacts correlate with the increase of the growth rates.

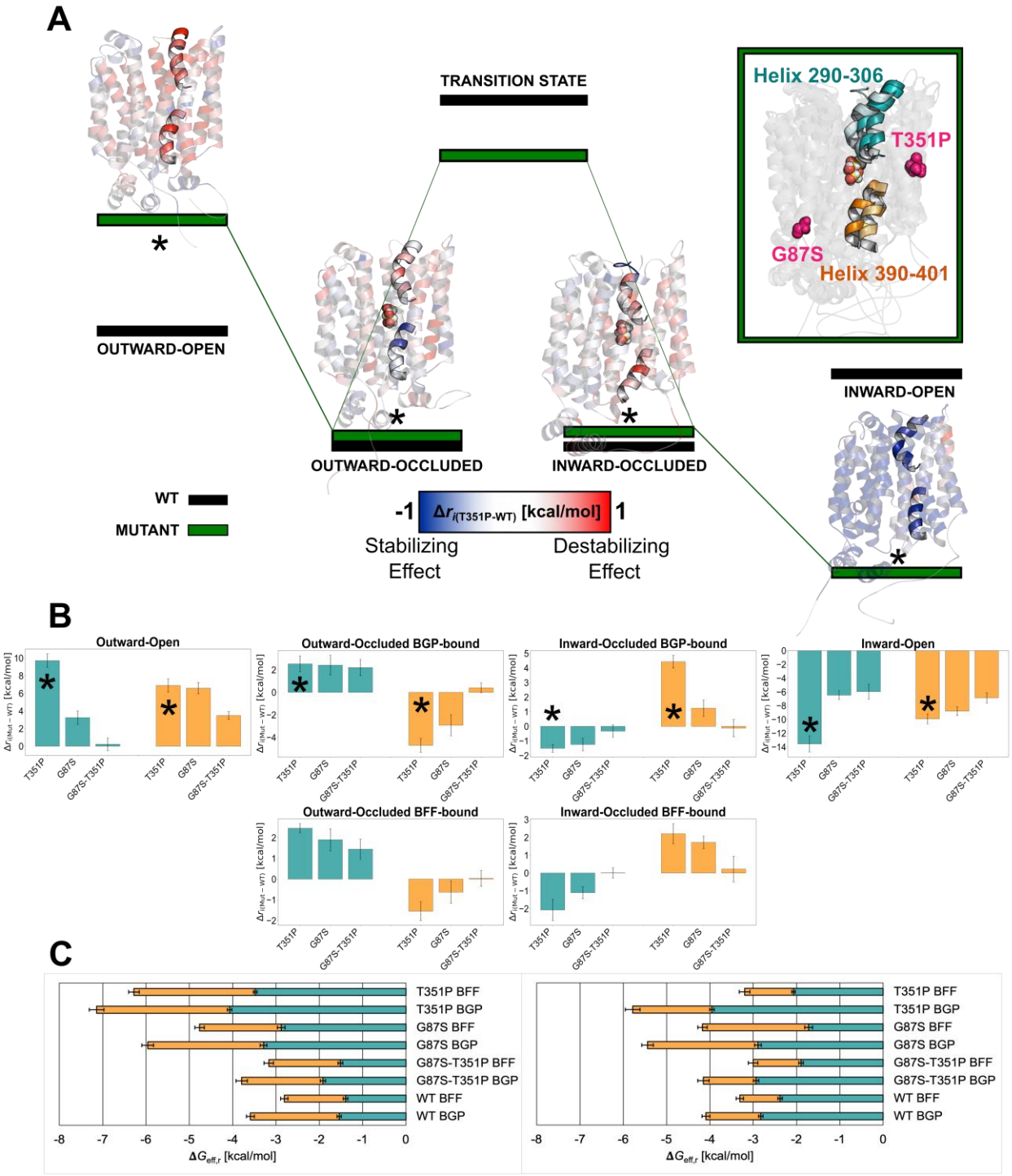

Fig. 4. Mutations impacting glucose (β-D-glucopyranose, BGP) and fructose (β-D-fructofuranose, BFF) transport exert an allosteric effect on two helices critical to MSF transporter function. (A) IolT1-mediated transport is modeled using the induced transition fit (ITF) mechanism, where substrate binding supplies energy for conformational changes, resembling substrate destabilization in enzyme catalysis. The wild-type IolT1 energy profile (black bars, [65]) and T351P mutation effects (green bars) show how T351P destabilizes helices 290-306 and 390-401 in the outward-open state and stabilize them in the inward-open state, facilitating substrate transport into the cell. The structural overlay of IolT1 highlights helix 290-306 (turquoise) and helix 390-401 (orange), with a gradient from outward- to inward-open states and the substrate (glucose), showing substitution sites G87S and T351P (magenta). (B)

The difference $\Delta r_{r,(Mutant-WT)}$ (eq. 3) across residues of helices 290-306 and 390-401 reveals that T351P has the greatest stabilizing effect, followed by G87S and G87S-T351P, correlating directly with cell growth trends. This stabilization effect is more pronounced with glucose than fructose. The asterisks (*) indicate the values depicted in panel A as per-residue contributions. (C) $\Delta G_{eff,r}$ sums per-residue contributions to effective binding energy for helices 290-306 and 390-401, in outward- (left) and inward-occluded (right) states, averaged from five replicas per variant, with error bars representing propagated SEM. For all variants, glucose binding shows more favorable binding, reinforcing the trend from panel B.

Characterization of ALE-derived xylose isomerase variants

ALE-mediated selection for improved $XylA_{AB}$ enzymes resulted in the formation of the $XylA_{AB}$-S2F variant and a cytosine to thymine (c_t) mutation 20 bp upstream of the start codon of *xylA* in pPREx2-$xylA_{AB}$ (Tab. 1). Mutations in the 5'-untranslated region (5'-UTR) and at the second amino acid position of recombinant proteins can influence gene expression levels, e.g. by stabilization of the mRNA or enhancing translation initiation complex formation [71-73]. Therefore, Western blot analysis was performed to test the effect of the $XylA_{AB}$-S2F and pPREx2(c_t) mutations on the XylA protein level. Both mutations led to a much higher protein content compared to wild-type $XylA_{AB}$ (Fig. S14A), suggesting that the improved growth of strains carrying these variants is due to higher glucose isomerase activity due to strongly increased XylA levels. An influence of the S2F mutation on the catalytic activity cannot be excluded but appears unlikely.

In the case of strain Fru^{neg} carrying pPREx2-$xylA_{XC}$, the three independent ALE experiments all led to the amino acid exchange W147S in $XylA_{XC.}$ This mutation had no obvious effect on the protein level compared to the native enzyme when analyzed by Western blotting (Fig. S14B). Since the presence of $XylA_{XC}$-W147S in addition to IolT1-G87S or IolT1-T351P in Fru^{neg} led to accelerated growth in fructose minimal medium (Fig. S2E-H, Fig. S3E-H), the W147S mutation should have a positive effect on the glucose isomerase activity of XylA. To test this assumption, His-tagged variants of $XylA_{XC}$ and $XylA_{XC}$-W147S were overproduced in *C. glutamicum* MB001(DE3) using plasmids pPREx5-$xylA_{XC}$ and pPREx5-$xylA_{XC}$-W147S and purified by Ni-NTA and size exclusion chromatography. Both proteins were purified as homodimers (Fig. S15).

Enzymatic activity was determined by a discontinuous colorimetric assay for glucose and xylose as substrates [74]. Native $XylA_{XC}$ revealed a 65-fold higher activity for xylose compared to glucose with catalytic efficiencies (k_{cat}/K_M) of 45.2 ± 8.1 $s^{-1}M^{-1}$ and 0.7 ± 0.1 $s^{-1}M^{-1}$, respectively (Tab. 3). For the $XylA_{XC}$-W147S enzyme, the k_{cat}/K_M for glucose increased by 8.4-fold to 5.9 ± 0.5 $s^{-1}M^{-1}$ while the k_{cat}/K_M for xylose decreased by 2.4-fold to 18.9 ± 1.1 $s^{-1}M^{-1}$, resulting in a diminished activity for xylose, only about thrice as high as the activity for glucose (Tab. 3). The results confirmed the strongly positive effect of the W147S mutation on the glucose isomerase activity of $XylA_{XC}$.

Table 3. Kinetic parameters of $XylA_{XC}$, $XylA_{XC}$-W147S and $XylA_{XC}$-G15A-W147S for the conversion of glucose and xylose.

Enzyme variant	Glucose			Xylose		
	k_{cat} (s^{-1})	K_M (mM)	k_{cat}/K_M (s^{-1} M^{-1})	k_{cat} (s^{-1})	K_M (mM)	k_{cat}/K_M (s^{-1} M^{-1})
$XylA_{XC}$	0.081 ± 0.003	116 ± 9	0.7 ± 0.1	1.48 ± 0.07	33 ± 5	45.2 ± 8.1
$XylA_{XC}$-W147S	0.43 ± 0.03	73 ± 12	5.9 ± 0.5	1.23 ± 0.05	65 ± 6	18.9 ± 1.1
$XylA_{XC}$-G15A-W147S	0.44 ± 0.01	67 ± 14	6.7 ± 1.4	1.08 ± 0.08	62 ± 5	17.6 ± 2.8

Directed evolution of $XylA_{XC}$-W147S and evaluation of mutations via MD simulations

Although W147S is probably the key mutation for improving the glucose isomerase activity of $XylA_{XC}$, we wondered if it is possible to identify mutations in addition to W147S that enhance the activity even further. For this purpose, we choose a selection system in which fructose uptake is not limiting due to the presence of IolT1-G87S, but glucose isomerase activity of $XylA_{XC}$-W147S is limiting due to an intentionally low expression level of the corresponding gene. When testing the growth of strain Fru^{neg}-$IolT1^{G87S}$ with plasmid pPREx2-*xylA*$_{XC}$-W147S in fructose minimal medium at varying IPTG concentrations, a Michaelis-Menten-like dependency was observed with a K_s value of 19.7 ± 2.4 µM IPTG at which half-maximal growth rate was achieved (Fig. S16).

This result confirmed that the growth rate of our selection strain correlates with the expression level of *xylA*$_{XC}$ and for our selection experiment, an IPTG concentration of 25 µM was chosen.

The *xylA*$_{XC}$-W147S gene was subjected to two rounds of random mutagenesis and the resulting variants were cloned into pPREx2 using *E. coli* DH5α as the host due to its higher transformation efficiency (Fig. 5A). The transformants were used to isolate a plasmid library for the transformation of *C. glutamicum* Fru^{neg}-IolT1^{G87S}. The transformed cells were plated on CGXII agar plates containing 40 g/L fructose, 25 µg/mL kanamycin and 25 µM IPTG (Fig. 5A). In total, 30 clones were obtained which revealed a bigger colony size compared to the unaltered control with non-mutated pPREx2-*xylA*$_{XC}$-W147S. Of these 30 clones, 24 showed faster growth also in liquid fructose minimal medium (Fig. S17). The plasmids of these 24 clones were isolated and sequenced. 18 clones carried between 1 and 4 missense mutations in the *xylA*-W147S coding region, 5 clones carried mutations in the *xylA* upstream region (Tab. S3). In total, 12 different missense mutations were obtained, the most frequent being S2N and S2T exchanges, each of which occurred four times, followed by two V5F and one V5I exchanges.

Excluding the S2 mutations, we individually tested nine of the missense mutations in combination with W147S in XylA$_{XC}$ for improved growth of Fru^{neg}-IolT1^{G87S} in a fructose minimal medium. Six of the nine mutations (R24A, E124K, S286T, L299M, A421V, T427M) barely affected growth, while two mutations (A9G, G15A) improved growth moderately, and one (V5F) strongly (Fig. 5B, Fig. 5C). As all these mutations were located in the N-terminal region, a translation-enhancing effect leading to increased XylA$_{XC}$ protein levels could be responsible for their positive effects on growth, similar to the S2F mutation found in the XylA$_{AB}$ protein (see above) [75]. In a Western blot analysis, all three mutations revealed a stronger protein signal compared to the XylA$_{XC}$-W147S variant (Fig. S18). Among the mutations, V5F improved the XylA$_{XC}$-W147S-mediated protein signal the most, followed by A9G and G15A. Since G15A is

located farthest away from the N-terminus and revealed a comparatively lower impact on expression, the $XylA_{XC}$-G15A-W147S protein was exemplarily purified and kinetically characterized. The additional G15A exchange improved the catalytic efficiency of $XylA_{XC}$-W147S for glucose from 5.9 ± 0.5 $s^{-1}M^{-1}$ to 6.7 ± 1.4 $s^{-1}M^{-1}$ while further reducing the same parameter for xylose from 18.9 ± 1.1 $s^{-1}M^{-1}$ to 17.6 ± 2.8 $s^{-1}M^{-1}$ (Tab. 3).

Fig. 5 (following page). Growth-based directed evolution of $XylA_{XC}$-W147S. (A) Experimental workflow for random mutagenesis of *xylA*$_{XC}$-W147S. Mutations were introduced via the GeneMorph II random mutagenesis kit (Agilent Technologies). Mutated *xylA*$_{XC}$ variants were cloned into pPREx2 and propagated in *E. coli* DH5α. Isolation of assembled plasmids and transformation of *C. glutamicum* Fru^{neg}-IolT1^{G87S} revealed faster growing clones on CGXII-fructose agar plates, which were then evaluated for growth in liquid fructose minimal medium in a BioLector system. Obtained mutated $XylA_{XC}$-W147S variants resulting in better growth were subsequently selected for further characterization via Western blot analysis for expression and/or xylose isomerase assays for protein activity determination. (B) Growth-based evaluation of novel *xylA*$_{XC}$ mutations obtained after random mutagenesis of *xylA*$_{XC}$-W147S. For this, novel *xylA*$_{XC}$ mutations were introduced separately into the pPREx2-*xylA*$_{XC}$-W147S plasmid. The newly constructed pPREx2 plasmids were then used for the transformation of *C. glutamicum* Fru^{neg}-IolT1^{G87S}. The growth experiment was performed in the BioLector XT at 30 °C and 1200 rpm in CGXII with 40 g/L of (w/v) fructose, 25 µg/mL kanamycin and 25 µM IPTG for 72 h. Inoculation was set to an OD_{600} of 1. (C) Growth rates of the strains shown in panel B, which were determined for the cultivation period from 24-34 h. All data points represent average values with standard deviations of three biological replicates.

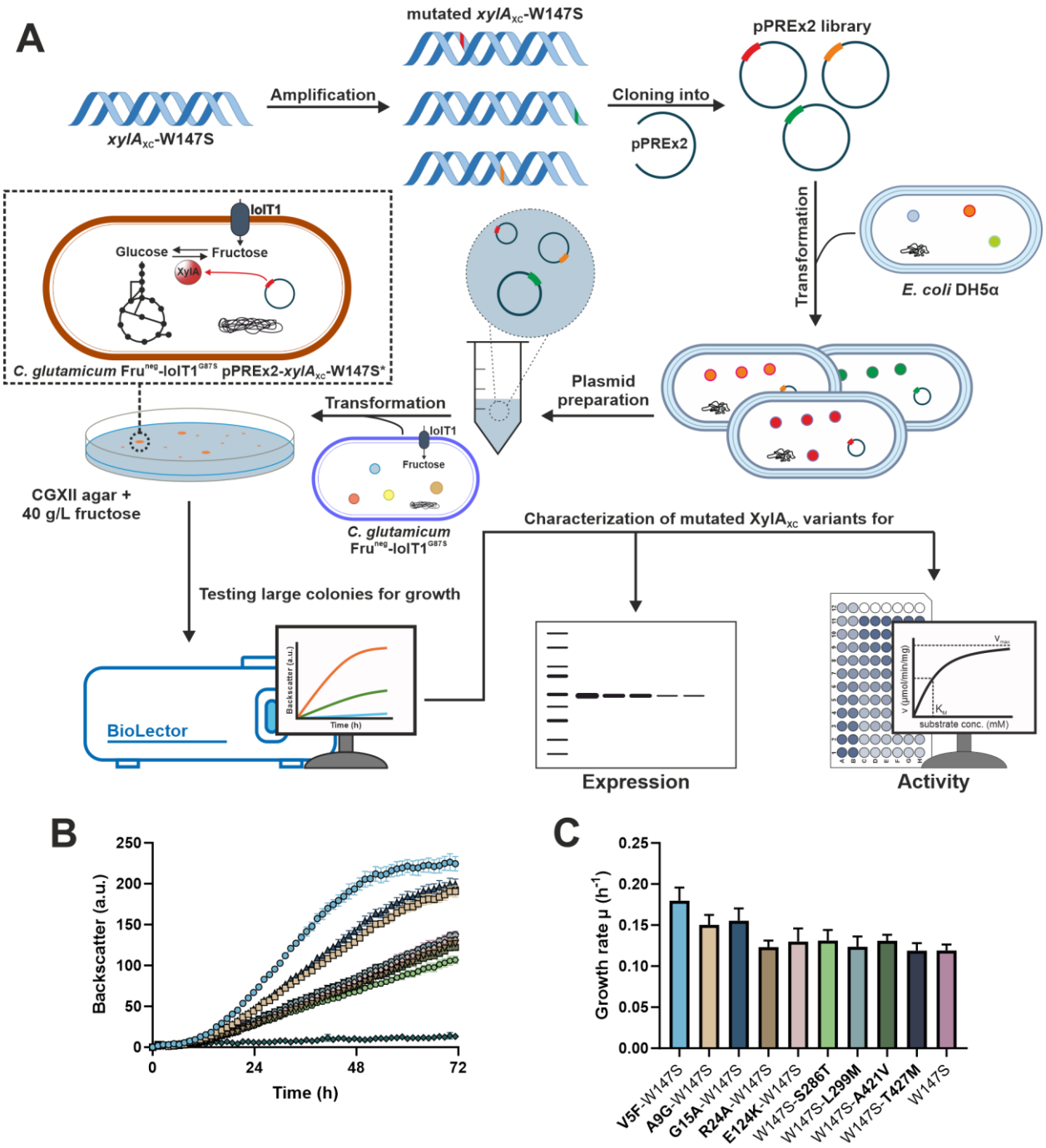

To explore the structural effect of substitutions W147S and G15A-W147S in XylA$_{XC}$ on glucose binding, we performed all-atom unbiased MD simulations of the structural homodimer model of XylA$_{XC}$ bound to glucose (as β-D-glucopyranose) (Fig. 6A, Fig. S19, Tab. S4). Starting

structures of the variants W147S and G15A-W147S were generated using the same protocol as for the IolT1 mutants. For the two systems, five replicas were simulated, each for 500 ns in length. Binding effective energy computations revealed that W147S favors the interactions of negatively charged residues with glucose-Mg^{2+} and disfavors interactions with polar and positively charged residues (Fig. 6B). Here, Mg^{2+} was considered part of the ligand as Mg^{2+} has been described as an activator binding together with the carbohydrate [76]. Tryptophan can be involved in carbohydrate-aromatic interactions [77,78], likely via C-H···π interactions [79,80], whereas cysteine is less frequently found near carbohydrates [77,78]. The distance of W147 to the carbohydrate atoms is ≥ 4 Å. As to position 147 only, the W to S exchange favors interactions with the carbohydrate only slightly (Fig. 6B). Yet, overall, the W147S substitution stabilizes the binding of glucose-Mg^{2+} compared to wild-type $XylA_{XC}$ ($\Delta\Delta G_{eff(W147S-WT)}$ = -7.1 ± 4.4 kcal/mol). The increased affinity to glucose probably favors the catalytic efficiency of the reversible conversion to fructose of $XylA_{XC}$. In contrast, the double substitution G15A-W147S does not markedly change the effective binding energy of glucose-Mg^{2+} to $XylA_{XC}$ compared to the W147S single mutation (Figure 6C), supporting that G15A may increase the XylA-mediated conversion through alternative mechanisms, such as alterations in gene expression. To conclude, substitution W147S is suggested to stabilize glucose-Mg^{2+} binding to $XylA_{XC}$, whereas the additional G15A substitution in the G15A-W147S variant does not affect the effective binding energy.

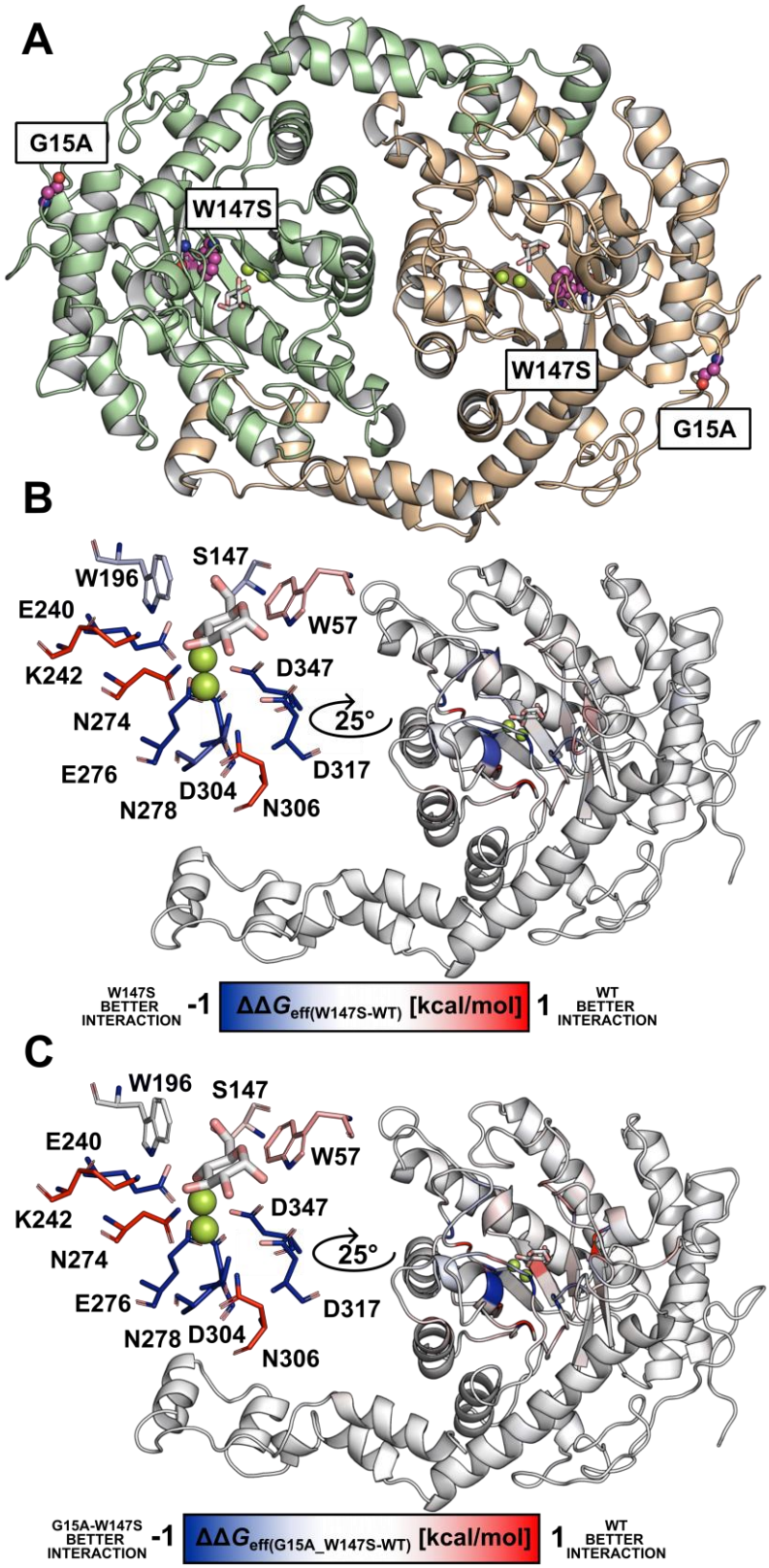
A
G15A
W147S
W147S
G15A
B
W196
S147
E240
W57
K242
D347
N274
25°
E276
D317
D304
N278
N306
W147S BETTER INTERACTION
-1
ΔΔG eff(W147S-WT) [kcal/mol]
1
WT BETTER INTERACTION
C
W196
S147
E240
W57
K242
D347
N274
25°
E276
D317
N278
D304
N306
G15A-W147S BETTER INTERACTION
-1
ΔΔG eff(G15A_W147S-WT) [kcal/mol]
1
WT BETTER INTERACTION

465

466

Fig. 6. Mutation W147S impacts glucose (β-D-glucopyranose, BGP)-Mg^{2+} binding to the XylA homodimer. (A) The homodimeric structure of *X. campestris* $XylA_{XC}$ was predicted using AlphaFold3 [81]. The structure contains glucose-Mg^{2+} in the respective binding site of each monomer (green and orange ribbons). Glucose is depicted as white-salmon sticks and Mg^{2+} as lemon spheres. The mutation sites G15A and W147S are shown as purple spheres. (B) Differential per-residue effective binding energy ($\Delta\Delta G_{eff(W147S-WT)}$) mapped at the structural level. The energies were averaged across replicas. Larger changes in contributions to the binding effective energy occur near the glucose-Mg^{2+} binding site but encompass residues up to 15 Å away from position 147. Residues for which the largest differences were found are depicted as sticks and colored according to the color scale; red and blue colors indicate stronger binding by wild-type $XylA_{XC}$ and the W147S variant, respectively. (C) Differential per-residue effective binding energy ($\Delta\Delta G_{eff(G15A-W147S-WT)}$) mapped at the structural level. The energies were averaged across replicas. Residues for which the largest differences were found are depicted as sticks and colored according to the color scale; red and blue colors indicate stronger binding by wild-type $XylA_{XC}$ and the G15A-W147S variant, respectively.

Construction of a glucose-negative *C. glutamicum* strain

The construction of a *C. glutamicum* strain capable of isomerizing glucose to fructose at mesophilic temperatures was the first step for the development of a strain capable of forming the low-caloric sweetener D-allulose from glucose. In the second step, the fructose-negative Fru^{neg} strain needed to be further metabolically engineered into a glucose-negative strain, which is incapable of utilizing glucose as the sole carbon source. Glucose is taken up as glucose 6-phosphate via PtsG, which is already absent in the Fru^{neg} strain. Like fructose, also glucose can be imported via IolT1 (see Fig. 3 and Tab. 2), but in contrast to fructose, *C. glutamicum* contains the endogenous glucokinases Glk (Cg2399) and PpgK (Cg2091) that phosphorylate glucose to glucose 6-phosphate, enabling its metabolization [50,51]. Therefore, the genes *glk* and *ppgK* and the gene *nanK* encoding *N*-acetylmannosamine kinase NanK (Cg2932) [82], which also accepts glucose as substrate [35], were deleted.

A growth experiment was performed with the strains Fru^{neg}-Δ*glk*Δ*ppgK* and Fru^{neg}-Δ*glk*Δ*ppgK*Δ*nanK* in glucose minimal medium. After a prolonged lag phase, suppressor mutants capable of utilizing glucose as a carbon source evolved for both strains (Fig. S20). Genome sequencing of three or two independently grown clones of both strains revealed that each one contained either a mutation in the *iolR* gene (cg0196) or in the *ihtR* gene (cg3388) (Tab. S5). In the

case of *iolR*, two identical mutations were identified, i.e. a cytosine insertion after nucleotide 483 causing a frameshift after codon 161. In the case of *ihtR*, tree different mutations were found, i.e. a guanine insertion after nucleotide 762 causing a frameshift after codon 254, a transposase insertion, and a missense mutation causing an L291R exchange. Both *iolR* and *ihtR* code for transcriptional regulators and are located in gene clusters that are involved in inositol metabolization (Fig. S21). IolR is a GntR-type regulator, which represses the expression of its downstream-located genes from *iolC* (cg0197) to *iolW* (cg0207) and also *iolT1* (cg0223) in the absence of *myo*-inositol (Fig. S21) [40]. IhtR is an IclR-type regulator, which was characterized as a repressor and linked to increased indole resistance via the regulation of its upstream gene *rhcM2* (cg3386), encoding a maleylacetate reductase [83]. Experiments in our lab provided strong evidence that IhtR also represses its downstream gene cluster *oxiC*-cg3390-*oxiD*-*oxiE* (unpublished data).

The mutations identified in *iolR* and *ihtR* are supposed to lead to inactive variants of these regulators, causing the derepression of their target genes. These include several genes encoding NAD^+-dependent inositol dehydrogenases, such as IolG, OxiE, and OxiD [39]. The IolG homolog of *Bacillus subtilis* was shown to oxidize not only *myo*-inositol, but also glucose to gluconate with reasonable activity (Ramaley et al., 1979). Such a side activity can explain the growth of the supressor mutants on glucose, as gluconate is good growth substrate for *C. glutamicum* [84]. We therefore deleted the gene clusters *iol1* and *iol2* (Ramp et al., 2021), and additionally *idhA3* (cg2313), encoding another inositol dehydrogenase (Ramp et al., 2022), in Fru^{neg}-Δ*glk*Δ*ppgK*Δ*nanK*, resulting in the Glu^{neg} strain. Even with a prolonged cultivation time of 100 h, the Glu^{neg} strain did not form suppressor mutants in glucose minimal medium (Fig. S22). Growth of the strain on glucose could be enabled by plasmid-based expression of *iolG*, *oxiE*, or *oxiD*, supporting that the corresponding inositol dehydrogenases are able to oxidize glucose to gluconate (Fig. S23).

Construction of a strain for the conversion of glucose to allulose based on strain Glu^{neg}

To convert glucose to allulose based on the Glu^{neg} strain, a suitable allulose 3-epimerase was required, which performs the epimerization of fructose to allulose efficiently in *C. glutamicum*. Two allulose 3-epimerases of *Agrobacterium tumefaciens* (Dae_{AT}) and *Arthrobacter globiformis* (Dae_{AG}) [85,86] and one tagatose 3-epimerase of *Pseudomonas cichorii* (Dte_{PC}) [87] were selected and initially tested in the Fru^{neg} strain for allulose formation from fructose in CGXII medium containing 20 g/L of glucose and 20 g/L of fructose. Of the selected enzymes, Dae_{AT} was most efficient in producing allulose from fructose, giving a titer of 4.18 ± 0.14 g/L allulose, corresponding to a yield of 22.3 ± 1.1 % (Fig. S24).

Next, we used strain Glu^{neg} for glucose to allulose conversion. Cultivations of Glu^{neg} strains were all conducted in CGXII medium with 10 g/L of gluconate for biomass formation and 30 g/L of glucose for allulose formation. Combined expression of $xylA_{XC}$ and dae_{AT} in strain Glu^{neg} revealed an allulose titer of 1.32 ± 0.07 g/L, corresponding to a yield of 4.1 ± 0.3 % from glucose (Fig. 7). By exchanging the native $XylA_{XC}$ enzyme with the evolved variants $XylA_{XC}$-W147S and $XylA_{XC}$-G15A-W147S, titers of 3.08 ± 0.12 and 3.17 ± 0.07 g/L were achieved, increasing the yield to 9.6 ± 0.4 % and 10.2 ± 0.2 %, respectively (Fig. 7). In a next step, glucose uptake was improved by introducing the G87S mutation into *iolT1* of strain Glu^{neg} resulting in strain Glu^{neg}-$IolT1^{G87S}$, which further elevated the allulose yield to 10.9 ± 0.4 %, resulting in a final titer of 3.45 ± 0.14 g/L allulose (Fig. 7). This yield is comparable to the one obtained in studies with purified enzymes, crude cell extract, or whole cells [14,88], but the microbial conversion requires considerably less preparation time and material. Unexpectedly, during the allulose production experiment, an increase of OD_{600} concomitant with accelerated consumption of glucose was observed for the producer strains in comparison to the empty vector controls (Fig. 7). Expression of the *xylA* gene

in strain Glu^{neg} or Glu^{neg}-IolT1^{G87S} was necessary for this behavior (Fig. S25, Fig. S26). This suggests, that the simultaneous presence of glucose and fructose enables partial utilization for growth despite the Glu^{neg} strain background.

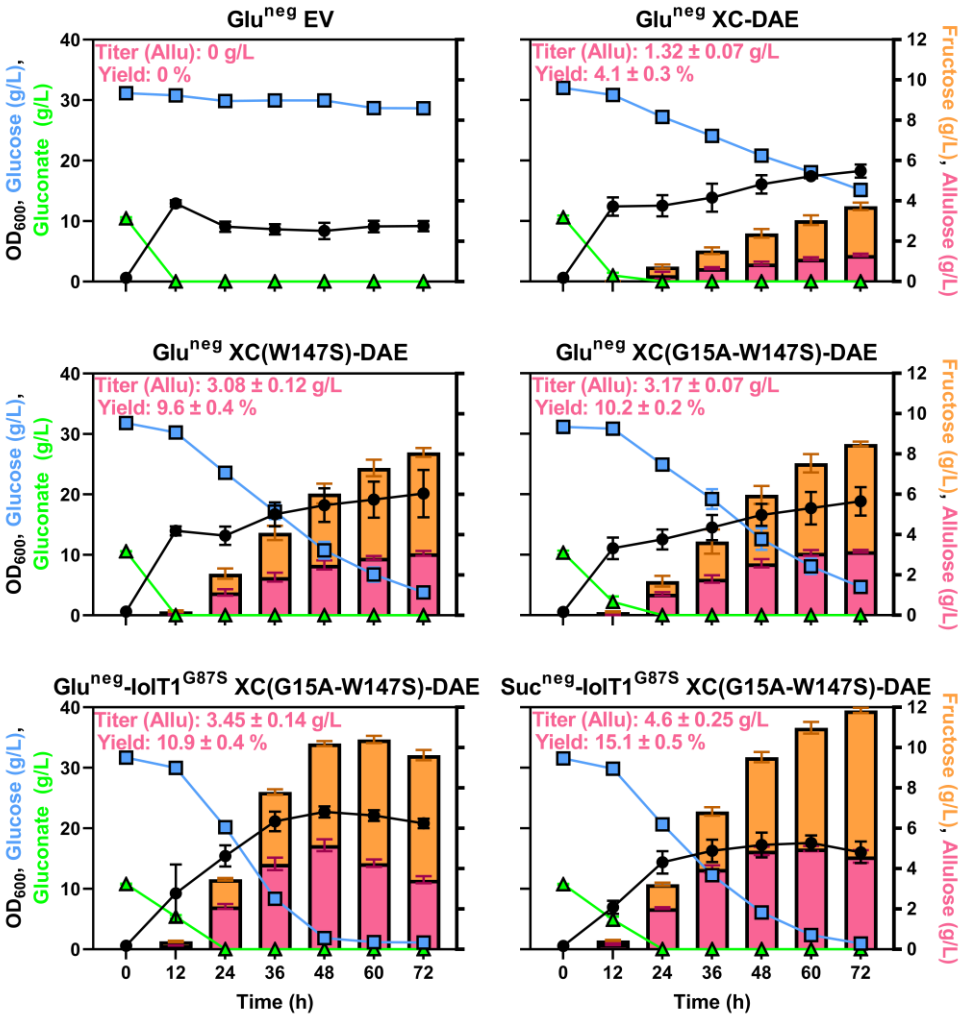

Fig. 7. Production of allulose from glucose by *C. glutamicum* MB001 Glu^{neg} and MB001 Glu^{neg} *iolT1*-G87S. The strains contained either pPREx2-*xylA*$_{XC}$-*dae*$_{AT}$ (XC-Dae$_{AT}$), pPREx2-*xylA*$_{XC}$-W147S-*dae*$_{AT}$ (XC-W147S-Dae$_{AT}$), pPREx2-*xylA*$_{XC}$-G15A-W147S-*dae*$_{AT}$ (XC-G15A-W147S-Dae$_{AT}$) or pPREx2 (EV). The experiment was conducted in CGXII medium with 10 g/L gluconate and 30 g/L glucose, 25 µg/mL kanamycin and 1 mM IPTG at 30°C and 130 rpm. Samples of the supernatant were taken every 12 h for a total of 72 h. Growth was measured via OD$_{600}$ and sugar concentrations were determined via HPLC. The data points represent average values with standard deviations of biological triplicates.

Identification of PtsS mutations presumably converting the sucrose transporter into a glucose-fructose transporter

To elucidate the reason for xylose isomerase-dependent slow growth on glucose of strain Glu^{neg}-IolT1^{G87S}, we performed an ALE to obtain clones with fast growth of the strain. In these experiments, the cultures were initially grown with 10 g/L gluconate as second carbon source besides 30 g/L glucose. Later gluconate content was first reduced to 2 g/L and eventually completely omitted (Fig. S27A). Fast growing clones were obtained for each of the two biological replicates of the ALE experiment (Fig. S27B, C). Genome sequencing of the clones revealed that both clones carried the identical mutation in the gene *ptsS* (cg2925), which encodes the sucrose-specific EII enzyme of the PEP-dependent phosphotransferase system: PtsS-A129G (Tab. S6). PtsS catalyzes the import of sucrose with simultaneous phosphorylation to sucrose 6-phosphate [45], which is subsequently converted by sucrose 6-phosphate hydrolase (Cg2927) to glucose 6-phosphate and fructose [89]. As *C. glutamicum* lacks a gene for sucrose synthase that might have formed sucrose from NDP-glucose and fructose, we assume that the mutations convert PtsS from a sucrose transporter to a glucose-fructose transporter forming glucose 6-phosphate and fructose within the cell. Glucose 6-phosphate can then be used as a growth substrate.

The A129G mutation found in PtsS was re-constructed in strain Glu^{neg}-IolT1^{G87S} expressing xylose isomerase and was shown to be beneficial for growth in glucose minimal medium, although it could not fully restore the growth rate of the evolved strains. Remarkably, the A129G mutation in PtsS prevented the growth of the strain in sucrose minimal medium, while enabling growth on glucose minimal medium after a prolonged lag phase, suggesting that the mutation inhibits the transport of sucrose by PtsS while presumably enabling the transport of glucose and fructose (Fig. S28).

We addressed the structural effect of A129G in PtsS on the geometry of the catalytic tunnel and on carbohydrate binding. We performed all-atom unbiased MD simulations [52] of the structural homodimer model of PtsS in the apo state and bound to glucose (as β-D-glucopyranose), fructose (as β-D-fructofuranose), glucose with fructose, and sucrose (Tab. S7). The mutation site A129G is ~10 Å away from the center of mass (COM) of the sucrose moiety (Fig. S29). Starting structures of the variant A129G were generated using the same protocol as for the IolT1 and the $XylA_{XC}$ mutants. For the two obtained systems, five replicas were simulated, each for 500 ns in length. A CAVER analysis [90] revealed that the mutation A129G does not markedly change the geometry of the catalytic tunnel when the tunnel is empty (Tab. S8). On the other hand, binding effective energy computations revealed that A129G favors interactions of the residues of the catalytic tunnel with glucose and glucose-fructose, whereas it does not affect fructose binding and disfavors sucrose binding (Fig. S29B). Based on these results, we assume that also wild-type PtsS has a limited ability to transport glucose and fructose, which is improved upon the introduction of A129G. Hence, the concomitant uptake of glucose and fructose seems responsible for glucose utilization of the Glu^{neg}-$IolT1^{G87S}$ strain in the presence of xylose isomerase.

To prevent this type of glucose utilization, we deleted the *ptsS* gene in Glu^{neg}-$IolT1^{G87S}$, which resulted in the construction of the Suc^{neg}-$IolT1^{G87S}$ strain. When expressing $xylA_{XC}$-G15A-W147S in this strain, a positive effect on allulose formation was observed, increasing its titer by 33% to 4.6 ± 0.25 g/L and its yield by 39% to 15.1 ± 0.5 % (Fig. 7).

Conclusion

We generated microbial strains that efficiently convert D-glucose to D-fructose at 30°C and epimerize fructose to the low-calorie natural sweetener D-allulose. In order to boost glucose-fructose interconversion by xylose isomerase, we employed *in vivo* selection with a strain whose

growth on fructose was strictly dependent on xylose isomerase activity. Via ALE we obtained xylose isomerase variants with an up to 10-fold increased catalytic efficiency. However, a second mutation was required to achieve fast growth of the selection strain, which was located in the sugar transporter IolT1 and improved sugar uptake 10-fold. For both the XylA and the IolT1 mutations, molecular dynamics studies shed light on the mechanistic effects of the amino acid exchanges. More generally, the IolT1 mutations illustrate the option to increase the velocity of a cytoplasmic enzyme reaction by increasing the substrate concentration via improved uptake. The establishment of a glucose-negative strain turned out to be much more challenging, as suppressor mutants rapidly evolved. They were able to utilize glucose via its oxidation to gluconate by the side-activity of inositol dehydrogenases, whose repression was knocked out by the suppressor mutations in transcriptional regulators. Deletion of the inositol dehydrogenase genes led to a glucose-negative strain. However, if this strain expresses xylose isomerase, it regained the ability to grow with glucose and our results suggest that this is due to a weak activity of the PTS sucrose transporter PtsS for simultaneous transport of glucose and fructose, coupled to the formation of glucose 6-phosphate. Additional deletion of the *ptsS* gene in the glucose-negative strain allowed the conversion of glucose to allulose with a yield of 15%, which corresponds to the one obtained with immobilized enzymes at high temperatures of about 60°C, but avoids enzyme purification and immobilization. In conclusion, we provide novel microbial catalysts for the efficient conversion of glucose and fructose at 30°C, for efficient conversion of glucose to D-allulose, and demonstrate the power of growth-based selection systems for the evolution of enzymes and transporters.

Material & Methods

Bacterial strains, plasmids and growth conditions

All bacterial strains and plasmids used in this work are listed in Table 1. Cloning was performed with *Escherichia coli* DH5α as host. Cultivation of *E. coli* was performed in lysogeny broth (LB) medium or on LB agar plates at 37°C with 50 µg/mL kanamycin, if cells were transformed with a plasmid. *C. glutamicum* was cultivated in brain heart infusion (BHI) medium or on BHI agar plates at 30°C, supplemented with 25 µg/mL and 15 µg/mL kanamycin if carrying a pPREx2 and pK19*mobsacB* plasmid, respectively.

Table 4. List of strains and plasmids used in this study

Strain or plasmid	Description	Reference
Strains		
E. coli DH5α	F^- φ80*lacZ*ΔM15 Δ(*lacZYA-argF*)*U169 recA1 endA1 hsdR17*(r_K^-, m_K^+) *deoR phoA supE44 thi*-1 *gyrA*96 *relA1* λ^-	[91]
C. glutamicum strains		
MB001	Prophage-free variant of the wild type ATCC 13032	[46]
MB001(DE3)	MB001 derivative with chromosomal integration of T7 RNA polymerase under control of P_{lacUV5}	[92]
Fru^{neg}	MB001 derivative with deletions of *ptsF* (cg2120) and *ptsG* (cg1537) and a *iolT1* (cg0223) promoter mutation preventing repression by IolR	This study
FXC	Fru^{neg} derivative with pPREx2-$xylA_{XC}$ evolved via adaptive laboratory evolution	This study
FAB	Fru^{neg} derivative with pPREx2-$xylA_{AB}$ evolved via adaptive laboratory evolution	This study
Fru^{neg}-IolT1^{G87S}	Fru^{neg} derivative with IolT1-G87S mutation	This study
Fru^{neg}-IolT1^{T351P}	Fru^{neg} derivative with IolT1-T351P mutation	This study
Fru^{neg}-Δ*glk*	Fru^{neg} derivative with *glk* (cg2399) deletion	This study
Fru^{negG}-Δ*glk*Δ*ppgK*	Fru^{neg}- Δ*glk* derivative with *ppgK* (cg2091) deletion	This study
Fru^{neg}-Δ*glk*Δ*ppgK*Δ*nanK*	Fru^{neg}-Δ*glk*Δ*ppgK* derivative with *nanK* (cg2932) deletion	This study
Glu^{neg}	Fru^{neg}-Δ*glk*Δ*ppgK*Δ*nanK* derivative with deletion of the gene clusters *iol1* (cg0196-cg0212) and *iol2* (cg3389-cg3393) and of *idhA3* (cg2313)	This study
Glu^{neg}-IolT1^{G87S}	Glu^{neg} derivative with IolT1-G87S mutation	This study
GXC	Glu^{neg}-IolT1^{G87S} derivative with pPREx2-$xylA_{XC}$-W147S evolved via adaptive laboratory evolution	This study

Glu^{neg}-IolT1^{G87S}-PtsS^{A129G}	Glu^{neg}-IolT1^{G87S} with PtsS-A129G mutation	This study
Glu^{neg}-IolT1^{G87S}-PtsS^{P328L}	Glu^{neg}-IolT1^{G87S} with PtsS-P328L mutation	This study
Suc^{neg}-IolT1^{G87S}	Glu^{neg}-IolT1^{G87S} with additional deletion of *ptsS* (cg2925)	This study
Plasmids		
pK19*mobsacB*	Kan^{R}, pK18 oriV$_{EC}$, *sacB*, *lacZα*, designed for genetic exchange in *C. glutamicum*	[93]
pK19*mobsacB*Δ*ptsF*	Kan^{R}, plasmid for *ptsF* (cg2120) deletion	This study
pK19*mobsacB*Δ*ptsG*	Kan^{R}, plasmid for *ptsG* (cg1537) deletion	This study
pK19*mobsacB*-P$_{06}$-*iolT1*	Kan^{R}, plasmid for mutation of *iolT1* (cg0223) promoter	[41]
pK19*mobsacB*-*iolT1*-G87S	Kan^{R}, plasmid for G87S mutation of *iolT1* (cg0223)	This study
pK19*mobsacB*-*iolT1*-T351P	Kan^{R}, plasmid for T351P mutation of *iolT1* (cg0223)	This study
pK19*mobsacB*Δ*glk*	Kan^{R}, plasmid for *glk* (cg2399) deletion	This study
pK19*mobsacB*Δ*ppgK*	Kan^{R}, plasmid for *ppgK* (cg2091) deletion	This study
pK19*mobsacB*Δ*nanK*	Kan^{R}, plasmid for *nanK* (cg2932) deletion	This study
pK19*mobsacB*Δ*iol1*	Kan^{R}, plasmid for *iol1* deletion covering cg0196-cg0212	[94]
pK19*mobsacB*Δ*iol2*	Kan^{R}, plasmid for *iol2* deletion covering cg3389-cg3393	[94]
pK19*mobsacB*Δ*idhA3*	Kan^{R}, plasmid for *idhA3* (cg2313) deletion	[39]
pK19*mobsacB*Δ*ptsS*	Kan^{R}, plasmid for *ptsS* (cg2925) deletion	This study
pK19*mobsacB*-*ptsS*-A129G	Kan^{R}, plasmid for A129G mutation in *ptsS* (cg2925)	This study
pK19*mobsacB*-*ptsS*-P328L	Kan^{R}, plasmid for P328L mutation in *ptsS* (cg2925)	This study
pPREx2	Kan^{R}, P$_{tacI}$, *lacI^{q}*, pBL1 *ori*$_{C.g.}$, pUC18 ColE1 *ori*$_{E.c.}$, consensus RBS (AAGGAG) for *C. glutamicum*	[48]
pPREx5	Kan^{R}, pPREx2 derivative with a His10-tag encoding sequence and a tobacco etch virus (TEV)-cleavage site	This study
pPREx2-*xylA*$_{AB}$	Kan^{R}, pPREx2 derivative containing xylose isomerase gene *xylA* of *Arthrobacter* strain N.R.R.L B3728 under the control of the *tac* promoter	This study
pPREx2-*xylA*$_{AG}$	Kan^{R}, pPREx2 derivative containing *xylA* of *Anoxybacillus gonensis* under the control of the *tac* promoter	This study
pPREx2-*xylA*$_{EC}$	Kan^{R}, pPREx2 derivative containing *xylA* of *E. coli* under the control of the *tac* promoter	This study
pPREx2-*xylA*$_{PE2}$	Kan^{R}, pPREx2 derivative containing *xylA* of *Piromyces* sp. E2 under the control of the tac promoter	This study
pPREx2-*xylA*$_{PR4}$	Kan^{R}, pPREx2 derivative containing *xylA* of *Paenibacillus* sp. R4 under the control of the *tac* promoter	This study
pPREx2-*xylA*$_{SM}$	Kan^{R}, pPREx2 derivative containing *xylA* of *Streptomyces murinus* under the control of the *tac* promoter	This study

pPREx2-*xylA*$_{XC}$	Kan^R, pPREx2 derivative containing *xylA* of *Xanthomonas campestris* under the control of the *tac* promoter	This study
pPREx2-*xylA*$_{AB}$-S2F	Kan^R, pPREx2-*xylA*$_{AB}$ derivative with S2F mutation in *xylA*$_{AB}$	This study
pPREx2(c_t)-*xylA*$_{AB}$	Kan^R, pPREx2-*xylA*$_{AB}$ derivative with cytosine to thymin mutation 20 bp upstream of the start codon	This study
pPREx2-*xylA*$_{XC}$-W147S	Kan^R, pPREx2-*xylA*$_{XC}$ derivative with W147S mutation in *xylA*$_{XC}$	This study
pPREx2-*dae*$_{AG}$	Kan^R. pPREx2 derivative with D-allulose 3-epimerase gene *dae* of *Arthrobacter globiformis*	This study
pPREx2-*dae*$_{AT}$	Kan^R, pPREx2 derivative with *dae* of *Agrobacterium tumefaciens*	This study
pPREx2-*dte*$_{PC}$	Kan^R, pPREx2 derivative with D-tagatose 3-epimerase gene *dte* of *Pseudomonas cichorii*	This study
pPREx2-*xylA*$_{XC}$-V5F-W147S	Kan^R. pPREx2-*xylA*$_{XC}$-W147S derivative with V5F mutation in *xylA*$_{XC}$	This study
pPREx2-*xylA*$_{XC}$-A9G-W147S	Kan^R. pPREx2-*xylA*$_{XC}$-W147S derivative with A9G mutation in *xylA*$_{XC}$	This study
pPREx2-*xylA*$_{XC}$-G15A-W147S	Kan^R. pPREx2-*xylA*$_{XC}$-W147S derivative with G15A mutation in *xylA*$_{XC}$	This study
pPREx2-*xylA*$_{XC}$-R24A-W147S	Kan^R. pPREx2-*xylA*$_{XC}$-W147S derivative with R24A mutation in *xylA*$_{XC}$	This study
pPREx2-*xylA*$_{XC}$-E124K-W147S	Kan^R. pPREx2-*xylA*$_{XC}$-W147S derivative with E124K mutation in *xylA*$_{XC}$	This study
pPREx2-*xylA*$_{XC}$-W147S-S286T	Kan^R. pPREx2-*xylA*$_{XC}$-W147S derivative with S286T mutation in *xylA*$_{XC}$	This study
pPREx2-*xylA*$_{XC}$-W147S-L299M	Kan^R. pPREx2-*xylA*$_{XC}$-W147S derivative with L299M mutation in *xylA*$_{XC}$	This study
pPREx2-*xylA*$_{XC}$-W147S-A421V	Kan^R. pPREx2-*xylA*$_{XC}$-W147S derivative with A421V mutation in *xylA*$_{XC}$	This study
pPREx2-*xylA*$_{XC}$-W147S-T427M	Kan^R. pPREx2-*xylA*$_{XC}$-W147S derivative with T427M mutation in *xylA*$_{XC}$	This study
pPREx2-*xylA*$_{XC}$-Strep	Kan^R, pPREx2-*xylA*$_{XC}$ derivative with Strep-tag fused to C-terminus of XylA$_{XC}$	This study
pPREx2-*xylA*$_{XC}$-W147S-Strep	Kan^R, pPREx2-*xylA*$_{XC}$-W147S derivative with Strep-tag fused to C-terminus of Xyl*A*$_{XC}$-W147S	This study
pPREx2-*xylA*$_{XC}$-V5F-W147S-Strep	Kan^R, pPREx2-*xylA*$_{XC}$-V5F-W147S derivative with Strep-tag fused to C-terminus of XylA$_{XC}$-V5F-W147S	This study
pPREx2-*xylA*$_{XC}$-A9G-W147S-Strep	Kan^R, pPREx2-*xylA*$_{XC}$-A9G-W147S derivative with Strep-tag fused to XylA$_{XC}$-A9G-W147S	This study
pPREx2-*xylA*$_{XC}$-G15A-W147S-Strep	Kan^R, pPREx2-*xylA*$_{XC}$-G15A-W147S derivative with Strep-tag fused to C-terminus of XylA$_{XC}$-G15A-W147S	This study
pPREx2-*xylA*$_{XC}$-*dae*$_{AT}$	Kan^R, pPREx2-*xylA*$_{XC}$ derivative with *dae* of *A. tumefaciens* downstream of *xylA*$_{XC}$	This study
pPREx2-*xylA*$_{XC}$-W147S-*dae*$_{AT}$	Kan^R, pPREx2-*xylA*$_{XC}$W147S derivative with *dae* of *A. tumefaciens* downstream of *xylA*$_{XC}$-W147S	This study

pPREx2-*xylA*$_{XC}$-G15A-W147S-*dae*$_{AT}$	Kan^R, pPREx2-*xylA*$_{XC}$-G15A-W147S derivative with *dae* of *A. tumefaciens* downstream of *xylA*$_{XC}$-G15A-W147S	This study
pPREx5-*xylA*$_{XC}$	Kan^R, pPREx5 derivative with *xylA* of *Xanthomonas campestris*	This study
pPREx5-*xlyA*$_{XC}$-W147S	Kan^R, pPREx5-*xylA*$_{XC}$ derivative with W147S mutation in *xylA*$_{XC}$	This study
pPREx5-*xylA*$_{XC}$-G15A-W147S	Kan^R, pPREx5-*xylA*$_{XC}$-W147S derivative with G15A mutation in *xylA*$_{XC}$	This study

Table 5. List of oligonucleotides used in this study

Oligonucleotide name	**Sequence (5'→3')**
Construction of pK19*mobsacB* plasmids	
ALP070_*ptsF*_FW1	CCTGCAGGTCGACTCTAGAGGACCACAACTTTCAGGTGGTAAC
ALP071_*ptsF*_RV1	GCCGGACAAGCGAGGAATTATTTAC
ALP072_*ptsF*_FW2	GTAAATAATTCCTCGCTTGTCCGGCGCAGCTGTAAACGCATAATC
ALP073_*ptsF*_RV2	AAAACGACGGCCAGTGAATTCTAACGGTGAGCTGCCAACATGAG
ALP078_*ptsG*_FW1	CCTGCAGGTCGACTCTAGAGCGACCCATCCAAGTACGGAATG
ALP079_*ptsG*_RV1	GTCGTCGTCAGTTTGGACGC
ALP080_*ptsG*_FW2	GCGTCCAAACTGACGACGACGTCAACGGCAAGAACGAGTAAC
ALP081_*ptsG*_RV2	AAAACGACGGCCAGTGAATTCAGAAGTACCAGATCAGAG
ALP086_*glk*_FW1	CCTGCAGGTCGACTCTAGAGCAACCATACCGTTCTGCCACC
ALP087_*glk*_RV1	CTGTAGTGGAAGCCAACTAGG
ALP088_*glk*_FW2	CCTAGTTGGCTTCCACTACAGGGCCGGTTTTTGTGGCATAAG
ALP089_*glk*_RV2	AAAACGACGGCCAGTGAATTGGTTATTGCCTCCACTCATGGG
ALP094_*ppgK*_FW1	CCTGCAGGTCGACTCTAGAGCCTCTTGTCATACTGCCAGGTC
ALP095_*ppgK*_RV1	CCACCGATATCAATTCCAAATCC
ALP096_*ppgK*_FW2	GGATTTGGAATTGATATCGGTGGCCAACACCTCACCCCATAAG
ALP097_*ppgK*_RV2	AAAACGACGGCCAGTGAATTCGACGCCGTCTTCATCTTC
ALP143_*nanK*_FW1	CCTGCAGGTCGACTCTAGAGTTCTCACCCGCACTCGTTCC
ALP144_*nanK*_RV1	GGTGCAAGTGGGATCAGTCATGAG
ALP145_*nanK*_FW2	CTCATGACTGATCCCACTTGCACCGCCCGCGATAACGCCTTTTAAGC
ALP146_*nanK*_RV2	AAAACGACGGCCAGTGAATTGTTGGGCTCTTAGAAGCGATTCTG
ALP255_T351P_FW	CCTGCAGGTCGACTCTAGAGGTCGCATTTCCGACAACTG
ALP256_T351P_RV	AAAACGACGGCCAGTGAATTGCTTGAAGCGCCACAAATGC
ALP336_G87S_FW	CCTGCAGGTCGACTCTAGAGATGGCTAGTACCTTCATTCAG
ALP337_G87S_RV	AAAACGACGGCCAGTGAATTATCGCATTGATGACAAAAGC
ALP478_*ptsS*_FW1	CCTGCAGGTCGACTCTAGAGCTATACCGCTCGACAGATCTTG
ALP479_*ptsS*_RV1	AATGTCGCGCAGGATGCGTTG
ALP480_*ptsS*_FW2	CAACGCATCCTGCGCGACATTTAAGTTGAAACCTTGAGTGTTCG
ALP481_*ptsS*_RV2	AAAACGACGGCCAGTGAATTCTGCTTTAGCATTTCCGGCACAG
ALP486_*ptsS*-A129G/P328L_FW	CCTGCAGGTCGACTCTAGAGATGGACCATAAGGACCTCGCGCAACG
ALP491_*ptsS*-A129G_RV1	AAAACGACGGCCAGTGAATTACTGGAGTGATCAGGAAGTC
ALP492_*ptsS*-P328L_RV1	AAAACGACGGCCAGTGAATTTTATGGTGTTGCTGGCACCGCTTC
Construction of pPREx2 plasmids	
ALP118_*xylA*(XC)_FW	CCTGCAGAAGGAGATATACAATGAGCAACACCGTTTTC

ALP121_*xylA*(XC)_RV	CTGTGGGTGGGACCAGCTAGCTTTCTCCTCTCAACGCGTCAG
ALP125_*xylA*(AG)_FW	CCTGCAGAAGGAGATATACAATGGCCTACTTCGAAAACGTGG
ALP126_*xylA*(AG)_RV	CTGTGGGTGGGACCAGCTAGTTAGCGAGCCACGCACACTTCC
ALP128_*xylA*(PE2)_FW	CCTGCAGAAGGAGATATACAATGGCCAAAGAATACTTCCC
ALP129_*xylA*(PE2)_RV	CTGTGGGTGGGACCAGCTAGTTACTGGTACATTGCCACGATTGC
ALP131_*xylA*(PR4)_FW	CCTGCAGAAGGAGATATACAATGGGCTACTTCGATCACGTGGG
ALP132_*xylA*(PR4)_RV	CTGTGGGTGGGACCAGCTAGTTACACGTTGATGATGTACTGGTTCAGG
ALP134_*xylA*(EC)_FW	CCTGCAGAAGGAGATATACAATGCAAGCCTATTTTGACCAGCTC
ALP135_*xylA*(EC)_RV	CTGTGGGTGGGACCAGCTAGTTATTTGTCGAACAGATAATGATTTACC
ALP137_*xylA*(AB)_FW	CCTGCAGAAGGAGATATACAATGTCCGTGCAGCCAACTCC
ALP138_*xylA*(AB)_RV	CTGTGGGTGGGACCAGCTAGTTAGCGGGAGCCCAGGAGGTGTTCGATTG
ALP140_*xylA*(SM)_FW	CCTGCAGAAGGAGATATACAATGTCCTTCCAGCCAACTCCAG
ALP141_*xylA*(SM)_RV	CTGTGGGTGGGACCAGCTAGTTAACCGCGTGCACCCAGGAG
ALP196_*dae*(AT)_FW	CCTGCAGAAGGAGATATACATATGAAGCACGGCATCTACTACTCC
ALP197_*dae*(AT)_RV	CTGTGGGTGGGACCAGCTAGTTAGCCACCGAGCACGAAGC
ALP200_*dae*(AG)_FW	CCTGCAGAAGGAGATATACATATGAAGATCGGCTGCCACG
ALP201_*dae*(AG)_RV	CTGTGGGTGGGACCAGCTAGTTAGTGCAGTTCGATGGTCTTG
ALP204_*dte*(PC)_FW	CCTGCAGAAGGAGATATACATATGAACAAGGTGGGCATGTTCTAC
ALP205_*dte*(PC)_RV	CTGTGGGTGGGACCAGCTAGTTATGCCAGCTTATCGCGCACGAAC
ALP223_AB(c_t)_FW	AAATGCATGCCGCTTCGCCTTC
ALP224_AB(c_t)_RV	GGACATATGTATATCTCCTTCTGCAGGCATGCAAGCTTGG
ALP248_AB(S2F)_FW	GGAGATATACATATGTTCGTGCAGCCAACTCC
ALP249_AB(S2F)_RV	GGAGTTGGCTGCACGAACATATGTATATCTCC
ALP359_RM_XC_FW	GCCTGCAGAAGGAGATATACAT
ALP360_RM_XC_RV	GTGGGACCAGCTAGCTTTCTCCTC
ALP368_*xylA*(XC)-*dae*(AT)_RV	CAGGTCAGCTGCAAAGGTGCTCAACGCGTCAGGTACTGATTG
ALP369_*xylA*(XC)-*dae*(AT)_FW	GCACCTTTGCAGCTGACCTGAAGGAGATATACATATGAAGCACGGCATCTACTAC
ALP428_V5F_FW1	CTGCAGAAGGAGATATACATATGAGCAACACCTTTTTC
ALP429_V5F/A9G/G15A_RV1	CAGAAGCTGTGCCAGTAGG
ALP430_V5F/A9G/G15A_FW2	GCCTACTGGCACAGCTTCTG
ALP431_E124K_FW	CGGACGACATCGGCGAGTACAAAAACAACCTCAAGCACATGGT
ALP432_E124K_RV	ACCATGTGCTTGAGGTTGTTTTTGTACTCGCCGATGTCGTCCG
ALP433_S286T_FW	ACGCTGTCGGGCCACACCTTCGAGCACGACCTG
ALP434_S286T_RV	CAGGTCGTGCTCGAAGGTGTGGCCCGACAGCGT
ALP435_L299M_FW	CAGCGATGCCGGCATGCTCGGCAGCATCG
ALP436_L299M_RV	CGATGCTGCCGAGCATGCCGGCATCGCTG
ALP437_A421V_RV	CTGGTGCCGTTGGCAAAGTC
ALP438_A421V_FW	GACTTTGCCAACGGCACCAG
Construction of pPREx5 plasmids	
ALP355_His-XC_FW	ACCTGTATTTTCAGGGCCATATGAGCAACACCGTTTTCATC
ALP356_His-XC_RV	CTGTCCACCAGTCATGCTAGTCAACGCGTCAGGTACTGATTG

Recombinant DNA work and construction of deletion mutants

All plasmids and oligonucleotides used in this study are listed in Table 4 and 5, respectively. All xylose isomerase (*xylA*), allulose 3-epimerase (*dae*) and tagatose 3-epimerase (*dte*) genes were

ordered in a codon-optimized form for *C. glutamicum* from Life Technologies (Carlsbad, USA). Standard cloning procedures such as PCR, DNA restriction and Gibson assembly were performed according to established protocols [95,96]. Transformation of *E. coli* was performed according to a standard heat-shock protocol [91], while transformation of *C. glutamicum* was conducted via electroporation [97]. Deletion of genes or integration of mutations into the genome of *C. glutamicum* were performed via double homologous recombination using pK19*mobsacB*-based plasmids [93]. Confirmation of deletions or mutations was obtained via colony PCR, using oligonucleotides annealing up- and downstream of the targeted genomic area. To verify the successful integration of mutations, the amplified colony PCR product was additionally sequenced. Expression of selected genes in *C. glutamicum* was performed with the vectors pPREx2 or pPREx5 using a *tac* promoter. The gene of interest was cloned downstream of the consensus ribosome binding site (RBS) of *C. glutamicum* of the respective plasmid. Gene expression was induced by addition of 1 mM or 25 µM isopropyl-β-D-thiogalactoside (IPTG).

Growth experiments in BioLector microcultivation systems

For micro-scale cultivations of *C. glutamicum*, the BioLector I, II or XT instruments (Beckman Coulter, Brea, USA) were used. Growth in this system was measured online as scattered light at 620 nm with a signal gain factor of 2, 4 or 10 with the BioLector I, II or XT, respectively [98]. Cultivations were performed in a 48-well FlowerPlate (Beckman Coulter, Brea, USA) by using defined CGXII medium [99] with 0.03 g/L protocatechuic acid and usually 40 g/L glucose, fructose or sucrose. If the strains carried expression plasmids, 1 mM IPTG and 25 µg/mL kanamycin were added to the medium. Inoculations were individually prepared to reach an initial OD_{600} of 0.5 or 5. BioLector cultivations were performed at 30°C, 1200 rpm and 85% humidity.

Adaptive laboratory evolution (ALE)

ALE experiments for the evolution of xylose isomerases were prepared in 24-well plates (Porvair Sciences, King's Lynn, UK) containing 5 ml CGXII medium with 40 g/L of fructose, 25 µg/mL kanamycin and 1 mM IPTG. The plates were shaken at 30°C and 900 rpm in a Multitron shaker (Infors HT, Einsbach, Germany). For evolution of the xylose isomerase of *Xanthomonas campestris* the first two transfers into fresh medium were performed after 5 days of cultivation with an initial OD_{600} of 7.5. Afterwards, the initial OD_{600} was lowered to 5 and the cultivation time was increased to 15 days. After three more consecutive cultivations, the experiment was stopped. For evolution of the xylose isomerase of *Arthrobacter* strain N.R.R.L B3728, the ALE was started at an OD_{600} of 5 with a cultivation time of 15 days. After three rounds of cultivation, the experiment was terminated. ALE experiments for the evolution of the Glu^{neg}-IolT1-G87S strain were performed in 100 mL baffled shake flasks. Initially, CGXII medium containing 10 g/L gluconate and 30 g/L glucose was used. The initial OD_{600} was set to 0.5 and the cultivation time to 3 days. After three rounds of cultivation, the medium composition was changed to 2 g/L gluconate and 30 g/L glucose for one cultivation of 3 days, whereupon the CGXII composition was again changed to solely 30 g/L of glucose for the last 3 days of cultivation.

Analysis of xylose isomerase protein levels

Investigation of intracellular protein levels was performed via semi-dry Western blot analysis. For this, C-terminally Strep-tagged protein variants of selected candidates were produced in the Fru^{neg} strain by using pPREx2 plasmid constructs (Tab. 4). Cultivation of strains was conducted in 100 mL baffled shake flasks containing 10 mL CGXII medium with 10 g/L of glucose, 25 µg/mL kanamycin and 1 mM IPTG for 24 h at 30°C and 130 rpm in a Minitron shaker (Infors HT, Einsbach, Germany). Cells were harvested at 4000 *g* for 30 min, resuspended in PBS and lysed via

ceramic beads homogenization in the Precellys® 24 (Avantor, Radnor, USA). Cell debris of whole cell lysates was removed via centrifugation at 20.000 *g* for 10 min to obtain soluble protein fractions. 100 µg of each protein fraction was separated via SDS-PAGE and blotted on a nitrocellulose membrane according to standard procedures [95]. After blocking unspecific and biotinylated protein binding to the membrane via a skim milk and avidin solution, respectively, Strep-tagged proteins were then visualized by a Strep-Tactin-HRP conjugate-based assay (IBA Lifesciences, Göttingen, Germany).

Production and purification of xylose isomerase variants

Production of $XylA_{XC}$ variants was achieved by using *C. glutamicum* MB001(DE3) strains carrying pPREx5 derivatives with the desired $xylA_{XC}$ variant. BHI medium was used for cultivation, which was inoculated to an OD_{600} of 0.5. Target gene expression was induced with 1 mM IPTG after 4 h of cultivation at 30°C and 130 rpm. After 24 h of cultivation, cells were harvested by centrifugation (4000*g*, 15 min, 4°C) and stored at -80°C for further use. For cell lysis, cells were resuspended in 4 mL lysis buffer (20 mM Tris-HCl pH 7.9, 500 mM NaCl, 5% (v/v) glycerol) per g cell wet weight containing cOmplete EDTA-free protease inhibitor (Roche, Basel, Switzerland) and lysed via the Multi Cycle Cell Disruptor (Constant Systems, Daventry, UK). Cell debris was removed via centrifugation (5000*g*, 30 min, 4°C) and filtration of the supernatant via Filtropur 0.2 µm filters (Sartorius, Göttingen, Germany). The soluble protein fraction was then loaded on a HisTrap HP column (GE Healthcare, Chicago, USA) and His-tagged proteins were eluted with 500 mM imidazole in elution buffer (20 mM Tris-HCl pH 7.9, 500 mM NaCl, 5% (v/v) glycerol, 500 mM imidazole). The resulting His-tagged $XylA_{XC}$ proteins were further purified by size exclusion chromatography using a Superdex 200 10/300 GL column (GE

Healthcare, Chicago, USA) via isocratic elution with enzyme assay buffer (200 mM $NaPO_4$ pH 7.5, 10 mM $MgCl_2$). Protein concentrations were determined with the Bradford assay [100].

Xylose isomerase activity assay

Xylose isomerase activity was detected by measuring fructose or xylulose formed by isomerization of glucose or xylose, respectively. For this, a molybdosilicate-dependent colorimetric assay was used [74], where the reduction of fructose or xylulose by Mo(VI) species resulted in a color change from yellow to blue, which was quantified at 750 nm with a Tecan Infinite M200 Pro microplate reader (Männedorf, Switzerland). The staining reaction was initiated by mixing samples obtained from the isomerization reaction with the 20-fold volume of reaction solution (50 mM Na_2SiO_3, 600 mM Na_2MoO_4, 0.95 M HCl pH 4.5) followed by incubation for 30 min at 70°C. For the isomerization reaction, samples with varying glucose (25-1000 mM) and xylose (5-750 mM) concentrations were prepared in enzyme assay buffer (200 mM $NaPO_4$ pH 7.5, 10 mM $MgCl_2$). The reaction was started by adding 25-50 µg of purified xylose isomerase for glucose isomerization and 0.5-10 µg for xylose isomerization. Each reaction was conducted in a final volume of 500 µL at 30°C for 24-48 h. Samples were taken after various time points over this period and mixed with 1/5 volume of 1 M HCl to quench the reaction. After the complete reaction was terminated, quenched samples were used for the colorimetric assay.

Random mutagenesis and selection via growth

Random mutagenesis was performed by using the GeneMorph II Random Mutagenesis Kit (Agilent Technologies, Santa Clara, USA) on $xylA_{XC}$ containing the W147S mutation. Conditions were framed to obtain a low mutation frequency of 0-4.5 mutations/kb by using 1000 ng of DNA template amplified with 30 PCR cycles. The resulting PCR products were purified using the DNA

Clean & Concentrator Kit (Zymo Research, Irvine, USA) and cloned via Gibson assembly into pPREx2 plasmid digested with NdeI and NheI [96]. Assembled plasmids were used for the transformation of *E. coli* DH5α and cells were plated on LB agar with 50 µg/mL kanamycin and incubated at 37°C for 24 h. The colonies formed were jointly resuspended in LB medium, which was then used for plasmid preparation via the Monarch Plasmid Miniprep Kit (New England Biolabs, Ipswich, USA). Purified plasmids were used for transformation of *C. glutamicum* Fru^{neg}-IolT1-G87S and cells were plated on CGXII agar plates with 40 g/L fructose, 25 µg/mL kanamycin and 25 µM IPTG. After 5 days of incubation at 30°C, larger sized clones were selected for a growth experiment in the BioLector.

Allulose production experiments

Production experiments for the conversion of either fructose or glucose to allulose were performed with 25 mL CGXII medium in 500 mL baffled shake flasks, which were incubated at 30°C and 130 rpm over 72 h. For cultivation of Fru^{neg} strains, overnight precultures were prepared in test tubes in BHI and CGXII medium with 20 g/L glucose and 25 µg/mL kanamycin. The main culture was prepared in CGXII medium with 20 g/L of glucose and 20 g/L of fructose, 1 mM IPTG and 25 µg/mL kanamycin. For Glu^{neg} strains, preparation of precultures was similar to Fru^{neg} strains, except that 20 g/L glucose was exchanged by 20 g/L gluconate in BHI and CGXII medium. Main cultures were prepared in CGXII medium with 10 or 15 g/L of gluconate and 30 g/L of glucose, 1 mM IPTG and 25 µg/mL kanamycin. In each case, cultivations were started by inoculating the medium to an initial OD_{600} of 0.5. Samples of the supernatant were taken after 12-24 h, used for OD_{600} measurement, filtered with 0.2 µm Whatman Puradisc 13 (Cytiva, Marlborough, USA) and stored at -20 °C for further usage.

Sugar quantification via HPLC

Filtered samples taken from the production experiments were diluted 1:4 or 1:8 with deionized water and used for HPLC analysis. Sugars such as fructose, glucose, and allulose were separated and quantified using a Carbo-Pb Guard Catridge (Phenomenex, Aschaffenburg, Germany) and a Metab-Pb 250 × 7.8 mm column (ISERA, Düren, Germany) in an Agilent LC-1100 system (Agilent Technologies, Santa Clara, USA). For each analysis, 5 µL of sample was injected into the system and separated at 80°C for 45 min with a flow rate of 0.6 mL/min with double-distilled water filtered through a 0.2 µm filter. A refraction index detector operating at 35°C was used for the detection of sugars. Sugar concentrations of samples were measured via a calibration curve, obtained from sugar standards with concentrations of 1 g/L, 2.5 g/L, 5 g/L, and 10 g/L of glucose, fructose and allulose.

Preparation of IolT1 starting structures

To our knowledge, there is no experimentally resolved 3D structure of IolT1 from *C. glutamicum* available. The starting structures for MD simulations of the different IolT1 states were thus modeled using TopModel [101] and the structures available in the Protein Data Bank [102] with PDB IDs 4ZWC, 4ZW9, 4JA3, and 4YB9 of the GLUT3 transporters in *H. sapiens*, the XylE transporter in *E. coli*, and the bovine GLUT5 transporter [65] as single templates for the outward-open, outward-occluded, inward-occluded, and inward-open conformations, respectively. The target sequence for IolT1 has Uniprot ID Q8NTX0 [103]. The quality of the models was assessed with TopScoreSingle (Tab. S2) [104].

The substitutions G87S, T351P, and G87S-T351P were introduced into IolT1 using FoldX [54], and the stability of the variants was evaluated in terms of the change in the folding free energy ($\Delta\Delta G$) with respect to the wildtype [105], as done for other bacterial membrane proteins [55]. Single

amino acid substitutions were performed 10 times for the respective residue and the results were averaged. If the average $\Delta\Delta G > 3$ kcal/mol, the substitution is considered destabilizing [56] and is not further pursued (Tab. S2).

In an aqueous solution of 20°C, D-fructose exists as an equilibrium of ~70% β-D-fructopyranose (BFP), ~23% of β-D-fructofuranose (BFF), and smaller percentages of the open chain and cyclic α-anomers [106]. Considering the low growth rate of cells containing IolT1 for D-fructose (Fig. 3), we hypothesized that this originates from the transport of BFF, which is less prevalent in solution. Accordingly, we prepared the BFF structure starting from its canonical SMILES using the fixpka option in OpenEye [107]. The most favorable conformer was generated using Omega 4.1.1.1 [108] and the flag -maxconfs = 1. BFF docking to IolT1 was performed using Autodock-3.0.5 [109] with the objective function DrugScore [110]. The selected pose represents the most populated cluster.

In an aqueous solution of 20°C, D-glucose exists as an equilibrium of ~36% α-D-glucopyranose (AGP) and ~64% β-D-glucopyranose (BGP) [111]. The more prevalent BGP structure is available in the Protein Data Bank (PDB ID 4ZW9) bound to human GLUT3 in the outward-occluded configuration [112]. After the superposition of the available protein structure with our generated model (RMSD = 0.3 Å), the bound pose of BGP was extracted and merged with the obtained model. Parallely, BGP was docked into the model, using the same protocol employed for BFF. The two BGP structures have a ligand dRMSD < 1.0 Å. We decided to use the BGP pose from the superpositioning and merging as the starting configuration.

The partial atomic charges of the two carbohydrate configurations were determined by first computing electrostatic potentials with Gaussian 16 [113] at the HF/6-31G level of theory and then performing a restrained fitting according to the RESP procedure [114,115]. The protonation states of

protein residues were adjusted according to pH 7.4 using the Epik routine [116-118] in Maestro [119]. The two unbound (outward-open, inward-open) and four bound (outward-occluded and inward-occluded, both with BGP and BFF) IolT1 conformations were embedded into a membrane composed of phosphatidylglycerol 16:0-18:1, cardiolipin 16:0-18.1, and phosphatidylinositol 16:0-18:1 in a ratio of 6:2:1 using the PPM server [53] and solvated using PACKMOL-Memgen [120,121]. The membrane composition resembles that of the native inner membrane of *C. glutamicum* [57,58]. A distance of at least 15 Å between the protein or membrane in the z-direction and the solvent box boundaries was kept. To obtain a neutral system, counter ions were added that replaced solvent molecules (KCl 0.15 M). A total of 16 independent starting configurations were generated and are listed in Tab. S2.

Preparation of the $XylA_{XC}$ starting structures

A resolved 3D structure of the XylA homodimer of *X. campestris* is not available. The starting structure for MD simulations of the homodimeric $XylA_{XC}$ state was thus modeled using AlphaFold3 [81]. The target sequence for $XylA_{XC}$ has Uniprot ID Q4UTU6 [122]. A fasta file with the two monomeric target sequences was prepared and uploaded to the server. The multiple sequence alignments were generated with the default AlphaFold3 workflow. Alphafold3 provides confidence scores in the form of a weighted linear combination of the predicted TM-score (pTM) and the interface predicted TM-score (ipTM). The five resulting models all have a pTM score of 0.82 and an ipTM score of 0.70. The less prevalent α-D-glucopyranose (AGP) structure bound to *S. rubiginosus* xylose isomerase in the monomeric configuration together with the coordinating Mg^{2+} ion is available in the Protein Data Bank (PDB ID 4LNC) [123]. We used PDB ID 2XIS to extract the information regarding the position of the second coordinating Mg^{2+} rather than the Mn^{2+} found in PDB ID 4LNC [124]. After the superposition of the experimental protein structures with our generated

model (RMSD = 1.9 Å), the bound pose of AGP – Mg^{2+} and the single Mg^{2+} were extracted and merged with the obtained model. Parallely, β-D-glucopyranose (BGP) was docked into the two monomers of the model, using the same protocol as for BFF. The AGP / BGP structures have a ligand dRMSD < 1.5 Å between the ligands with respect to both monomers. We decided to use the docked BGP pose and the Mg^{2+} from the superpositioning step to generate the starting configuration.

The substitutions W147S and G15A-W147S were introduced in XylA following the same protocol as described for the IolT1 mutations. The partial atomic charges of the ligands were taken from the IolT1 setup. The obtained systems were solvated using PACKMOL-Memgen [120,121]. To obtain a neutral system, counter ions were added that replaced solvent molecules (KCl 0.15 M). Two independent starting configurations were generated and are listed in Tab. S4**.**

Preparation of the PtsS starting structure

To our knowledge, there is also no experimentally resolved 3D structure of the sucrose phosphotransferase PtsS from *C. glutamicum*. The starting structure for MD simulations of the homodimeric PtsS state was thus modeled using AlphaFold3 [81]. The target sequence for PtsS has Uniprot ID Q8NMD6 [103]. A fasta file with the two monomeric target sequences was prepared and uploaded to the server. The multiple sequence alignments were generated with the default AlphaFold3 workflow. The five resulting models all have a pTM score of 0.57 and an ipTM score of 0.59. The structure of 2-acetamido-2-deoxy-β-D-glucopyranosyl-(1→4)-2-acetamido-2-deoxy-β-D-glucopyranose is available in the Protein Data Bank (PDB ID 3QNQ) bound to the *B. cereus* phosphorylation-coupled saccharide transporter in the homodimeric configuration [125]. After the superposition of the experimental protein structure with our generated model (RMSD = 2.7 Å), the carbohydrate pose was extracted and merged with the obtained model. Additionally, β-D-

glucopyranose (BGP), β-D-fructofuranose (BFF), sucrose (SUC), and BGP and BFF together (BGP/BFF) were docked into the two monomers of the model, using the same protocol as before and the bound carbohydrate pose to generate the docking grid. BGP/BFF corresponds to the SUC moiety but without a bond between between the two monosaccharides. The carbohydrate structures have a ligand dRMSD < 1.5 Å with respect to both monomers.

The substitution A129G was introduced in PtsS following the same protocol as described for the IolT1 mutations. The partial atomic charges of the ligands were taken from the IolT1 setup. The obtained systems were embedded into a membrane composed of phosphatidylglycerol 16:0-18:1, cardiolipin 16:0-18.1, and phosphatidylinositol 16:0-18:1 in a ratio of 6:2:1 using the PPM server [53] and solvated using PACKMOL-Memgen [120,121] as for IolT1. Two independent starting configurations were generated and are listed in Tab. S7**.** To check if the proposed substitutions would modify the geometry of the binding site tunnel, the bottleneck radius and the length of the wild type and the variant tunnels were calculated using CAVER 3.0 [90] (Tab. S8). The COMs of the residues in a distance < 3.0 Å from the original 2-acetamido-2-deoxy-β-D-glucopyranosyl-(1→4)-2-acetamido-2-deoxy-β-D-glucopyranose were defined as the starting points of the search. The probe radius was set to 1.2 Å.

Unbiased molecular dynamics (MD) simulations of IolT1 configurations, XylA$_{XC}$ and PtsS

The GPU particle mesh Ewald implementation from the AMBER23 suite of molecular simulations programs [126] with the ff19SB [127], Lipid21 [128], and the GLYCAM-06j [129] forcefields for the protein, membrane lipids, and carbohydrate ligands, respectively, were used; water molecules and ions were parametrized using the OPC3POL model [130,131] and the Li and Merz 12-6 ions parameters [132-134]. For each configuration in Tab. S2 and Tab. S4, five independent MD simulations of 500 ns length were performed. Covalent bonds to hydrogens were constrained with the SHAKE algorithm

[135], and the hydrogen masses were repartitioned [136], allowing the use of a time step of 4 fs. Details of the thermalization of the simulation systems are given below. All unbiased MD simulations of IolT1 showed structurally rather invariant protein structures and membrane phases as evidenced by electron density calculations (Fig. S5-10). The overall nofit-RMSD of β-D-glucopyranose (BGP) and β-D-fructofuranose (BFF) revealed structurally stable binding poses across different replicas for the outward-occluded and inward-occluded configurations (Fig. S11). The unbiased MD simulations of $XylA_{XC}$ yielded structurally rather invariant protein structures (Fig. S19) and stable binding poses of the ligands (Fig. S19**)**. All unbiased MD simulations of PtsS showed structurally rather invariant protein structures and membrane phases as evidenced by electron density calculations (Fig. S30, Fig. S31). The overall nofit-RMSD of BGP, BFF, sucrose and BGP/BFF revealed structurally stable binding poses across different replicas for the wild type and A129G mutant configurations (Fig. S32).

Relaxation, thermalization, and production runs of the obtained systems

An initial minimization step was performed with the CPU code of pmemd [137]. Each minimization was organized in four steps of 10000 cycles each, for a total of 40000 cycles of minimization. Afterward, each minimized system was thermalized in one stage from 0 to 300 K over 250 ps using the NVT ensemble and the Langevin thermostat [138], and the density was adapted to 1.0 g cm^{-3} over 750 ps using the NPT ensemble with a semi-isotropic Berendsen barostat [139], with the pressure set to 1 bar. The thermalization and equilibration were performed with the GPU code of pmemd [137]. There are four density adaptation steps with a total time of 1 ns. The sum of thermalization, density adaptation, and equilibration took 50 ns. For each replica, 500 ns of production run using the GPU code of pmemd was performed in the NPT ensemble at a temperature of 300 K using the Langevin thermostat [138] and a collision frequency of 1 ps^{-1}. To avoid noticeable distortions in the simulation

box size, semi-isotropic pressure scaling using the Berendsen barostat [139] and a pressure relaxation of 1 ps was employed by coupling the box size changes along the membrane plane [140].

Constraint network analysis

To detect changes in structural rigidity between IolT1 wildtype and variants, we analyzed ensembles of constraint network topologies based on conformational ensembles saved every 400 ps from the production phase of the unbiased MD simulations. For each configuration, we generated 400 conformations. Overall, we investigated 1,600 conformations in this study.

Structural rigidity was analyzed with the CNA software package [59,141], which is a front and back end to the FIRST software [142]. It was used to construct networks of nodes (atoms) and covalent and noncovalent (hydrogen bonds, salt bridges, and hydrophobic tethers) constraints. The hydrogen bond energy (including salt bridges) is determined from an empirical function [143], while hydrophobic tethers between carbon and sulfur atoms were considered if the distance between these atoms was less than the sum of their van der Waals radii plus a cutoff of 0.25 Å [144].

Biomolecules generally display a hierarchy of rigidity that reflects the modular structure of biomolecules in terms of secondary, tertiary, and supertertiary structure [141]. This hierarchy can be identified by gradually removing noncovalent constraints from an initial network representation of a biomolecule, which generates a succession of network states σ, resulting in a "constraint dilution trajectory". For that, hydrogen bonds and salt bridges are removed in the order of increasing strength such that for network state σ, only those hydrogen bonds are kept that have an energy $E_{HB} \leq E_{cut}(\sigma)$. In our analysis, we used energy cutoffs between E_{start} = -0.1 kcal/mol and E_{stop} = -10.0 kcal/mol, with E_{step} = 0.1 kcal/mol. We also assigned the cutoff for finding native contacts between pairs of residues (ncd = 4.5).

For all MD-generated snapshots, we calculated a rigidity index r_{i} [61] (eq. 1).

$$r_i = min\{E_{cut} | \exists c \in C^{E_{cut}} : A_{i1} \wedge A_{i2} \in c\} \quad \text{(eq. 1)}$$

The index is defined for each covalent bond *i* between two atoms A_i,[102] as the E_{cut} value during a constraint dilution simulation at which the bond changes from rigid to flexible. Phrased differently, this index monitors when a bond segregates from any rigid cluster *c* of the set of rigid clusters C^{Ecut}. It reflects structural stability on a per-residue basis and, thus, can be used to identify the location and distribution of structurally weak or strong parts in IolT1.

The same analysis was performed for the five independent replicas of each IolT1 configuration for the WT, the G87S and T351P single variants, and the G87S-T351P double variant. The per-residue r_i values were averaged on a per-residue basis across the five replicas and the SEM was calculated. Afterward, the per-residue difference $\Delta r_{i,(Mut-WT)}$ (eq. 2) was calculated, including an error propagation analysis for the SEM. Values of $\Delta r_{i,(Mut-WT)} < 0$ (> 0) indicate that the variant is more rigid (flexible) than the wildtype.

$$\Delta r_{i,(Mut-WT)} = r_{i,(Mut)} - r_{i,(WT)} \quad \text{(eq. 2)}$$

Finally, we obtained the cumulative difference $\Delta r_{r,(Mut-WT)}$ of a specific region of interest, r_r (residues 290-306 and residues 390-401) (eq. 3) by summing the *m* single per-residue $r_{i,(Mut-WT)}$ contributions, including an error propagation analysis.

$$\Delta r_r = \sum_i^m \Delta r_{i,(Mut-WT)} \quad \text{(eq. 3)}$$

MM-PBSA calculations to assess β-D-glucopyranose (BGP)/β-D-fructofuranose (BFF) binding to IolT1, BGP binding to XylA$_{XC}$, and carbohydrate binding to PtsS

MM-PBSA (Molecular Mechanics Poisson-Boltzmann Surface Area) calculations were conducted to determine the binding effective energy of BGP/BFF binding to IolT1, BGP binding to XylA$_{XC}$, and the binding of multiple carbohydrates to PtsS. These calculations were performed for IolT1,

$XylA_{XC}$, and PtsS in the wildtype state and the proposed mutants, utilizing the trajectories from unbiased MD simulations. Ligand binding poses were identified as those exhibiting an RMSD < 1.5 Å compared to the first frame of each respective production run. To compute the average binding effective energy of each ligand with the respective system within the ensemble of the unbiased MD frames, we employed MMPBSA.py [145]. This was done using dielectric constants of 1.0 for the protein and 80.0 for the solvent. For IolT1, the cumulative binding effective energy of two specific regions of interest ($\Delta G_{eff,r}$ for residues 290-306 and residues 390-401) was also calculated. For $XylA_{XC}$ and PtsS, the binding effective energy computations were performed for the two monomers, and the results were averaged. The computations were converged, as evidenced by the comparison between the first and second halves of the trajectories (Fig. S33, Fig. S34).

Funding

This project was funded by the Bundesministerium für Bildung und Forschung (BMBF) within the project IMPRES-2 (FKZ 031B1054B), grant to M.B., and, in part, by the Deutsche Forschungsgemeinschaft (DFG, German Research Foundation), project 267205415/CRC1208, grant to H.G. (subproject A03), and, in part, by a grant from the Ministry of Innovation, Science, and Research within the framework of the NRW Strategieprojekt BioSC (No. 313/323-400-002 13).

Acknowledgments

We are grateful for computational support from the "Zentrum für Informations und Medientechnologie" at the Heinrich-Heine-Universität Düsseldorf and the computing time provided by the John von Neumann Institute for Computing (NIC) to H.G. on the supercomputer JUWELS at the Jülich Supercomputing Centre (JSC) (user IDs: VSK33, T1SS).

References

1. Speck, J.C. The Lobry de Bruyn-Alberda van Ekenstein transformation. *Adv Carbohydr Chem* **13**, 63-103 (1958).
2. Sowden, J.C. & Schaffer, R. The reaction of D-glucose, D-mannose and D-fructose in 0.035 N sodium hydroxide at 35 °C. *J Am Chem Soc* **74**, 499-504 (1952).
3. Marshall, R.O. & Kooi, E.R. Enzymatic conversion of D-glucose to D-fructose. *Science* **125**, 648-649 (1957).
4. Hanover, L.M. & White, J.S. Manufacturing, composition, and applications of fructose. *Am J Clin Nutr* **58**, 724-732 (1993).
5. Bhosale, S.H., Rao, M.B. & Deshpande, V.V. Molecular and industrial aspects of glucose isomerase. *Microbiol Mol Biol Rev* **60**, 280-300 (1996).
6. Parker, K., Salas, M. & Nwosu, V.C. High fructose corn syrup: Production, uses and public health concern. *Biotechnol Mol Biol Rev* **5**, 71-78 (2010).
7. Tewari, Y.B. & Goldberg, R.N. Thermodynamics of the conversion of aqueous glucose to fructose. *J Solution Chem* **13**, 523-547 (1984).
8. Zhu, G.P. *et al.* Increasing the thermostability of D-xylose isomerase by introduction of a proline into the turn of a random coil. *Protein Eng* **12**, 635-638 (1999).
9. Dekker, K., Yamagata, H., Sakaguchi, K. & Udaka, S. Xylose (glucose) isomerase gene from the thermophile *Thermus thermophilus*: cloning, sequencing, and comparison with other thermostable xylose isomerases. *J Bacteriol* **173**, 3078-3083 (1991).
10. Vieille, C., Hess, J.M., Kelly, R.M. & Zeikus, J.G. *xylA* cloning and sequencing and biochemical characterization of xylose isomerase from *Thermotoga neapolitana*. *Appl Environ Microbiol* **61**, 1867-1875 (1995).
11. OECD/FAO. OECD-FAO Agricultural Outlook 2021-2030. *OECD Publishing* (2021).
12. Beerens, K. *et al.* Biocatalytic synthesis of the rare sugar kojibiose: process scale-up and application testing. *J Agric Food Chem* **65**, 6030-6041 (2017).
13. Huang, J. *et al.* Production of D-mannose from D-glucose by co-expression of D-glucose isomerase and D-lyxose isomerase in *Escherichia coli*. *J Sci Food Agric* **98**, 4895-4902 (2018).
14. Chen, X. *et al.* One pot cascade biosynthesis of D-allulose from D-glucose and its kinetic modelling. *Chem Eng Sci* **248**, 117167 (2022).
15. Wagner, N., Bosshart, A., Failmezger, J., Bechtold, M. & Panke, S. A separation-integrated cascade reaction to overcome thermodynamic limitations in rare-sugar synthesis. *Angew Chem Int Ed Engl* **54**, 4182-4186 (2015).
16. Hossain, A. *et al.* Rare sugar D-allulose: Potential role and therapeutic monitoring in maintaining obesity and type 2 diabetes mellitus. *Pharmacol Ther* **155**, 49-59 (2015).
17. Jiang, S. *et al.* Review on D-allulose: *in vivo* metabolism, catalytic mechanism, engineering strain construction, bio-production technology. *Front Bioeng Biotechnol* **8**, 26 (2020).
18. Daniel, H., Hauner, H., Hornef, M. & Clavel, T. Allulose in human diet: the knowns and the unknowns. *Br J Nutr* **128**, 172-178 (2022).
19. Moura, F. Scientific review of the evidence on the metabolism, caloric value, glycemic response, and cariogenic potential of allulose. *Memorandum FDA Administrative File* **10**(2020).
20. Koch, T.J., Kipping, F., Butz, S., Lesch, M. & Hässler, T. Synthesis of D-allulose. *Patent Application Publication US 2019 / 0315790 A1* (2019).

21. Zhang, W., Yu, S., Zhang, T., Jiang, B. & Mu, W. Recent advances in D-allulose: physiological functionalities, applications, and biological production. *Trends Food Sci* **54**, 127-137 (2016).
22. Meng, M., Lee, C., Bagdasarian, M. & Zeikus, J.G. Switching substrate prefernce of thermophilic xylose isomerase from D-xylose to D-glucose by redesigning the substrate binding pocket. *Proc Natl Acad Sci USA* **88**, 4015-4019 (1991).
23. Lönn, A., Gárdonyi, M., Van Zyl, W., Hahn-Hägerdal, B. & Otero, R.C. Cold adaptation of xylose isomerase from *Thermus thermophilus* through random PCR mutagenesis. *Eur J Biochem* **269**, 157-163 (2002).
24. Sriprapundh, D., Vieille, C. & Zeikus, J.G. Directed evolution of *Thermotoga neapolitana* xylose isomerase: high activity on glucose at low temperature and low pH. *Protein Eng* **16**, 683-690 (2003).
25. Romero, P.A. & Arnold, F.H. Exploring protein fitness landscapes by directed evolution. *Nat Rev Mol Cell Biol* **10**, 866-876 (2009).
26. Lee, S.-M., Jellison, T. & Alper, H.S. Directed evolution of xylose isomerase for improved xylose catabolism and fermentation in the yeast *Saccharomyces cerevisiae*. *Appl Environ Microbiol* **78**, 5708-5716 (2012).
27. Seike, T. *et al.* Molecular evolutionary engineering of xylose isomerase to improve its catalytic activity and performance of mico-aerobic glucose/xylose co-fermentation in *Saccharomyces cerevisiae*. *Biotechnol Biofuels* **12**, 139 (2019).
28. Dragosits, M. & Mattanovich, D. Adaptive laboratory evolution - principles and applications for biotechnology. *Microb Cell Fact* **12**, 64 (2013).
29. Sandberg, T.E., Salazar, M.J., Weng, L.L., Palsson, B.O. & Feist, A.M. The emergence of adaptive laboratory evolution as an efficient tool for biological discovery and industrial biotechnology. *Metab Eng* **56**, 1-16 (2019).
30. Eggeling, L. & Bott, M. A giant market and a powerful metabolism: L-lysine provided by *Corynebacterium glutamicum*. *Appl Microbiol Biotechnol* **99**, 3387-3394 (2015).
31. Becker, J. & Wittmann, C. Bio-based production of chemicals, materials and fuels - *Corynebacterium glutamicum* as versatile cell factory. *Curr Opin Biotechnol* **23**, 631-640 (2012).
32. Wendisch, V.F., Jorge, J.M.P., Perez-Garcia, F. & Sgobba, E. Updates on industrial production of amino acids using *Corynebacterium glutamicum*. *World J Microbiol Biotechnol* **32**, 105 (2016).
33. Eggeling, L. & Bott, M. Handbook of *Corynebacterium glutamicum*. *CRC Press, Taylor & Francis Group* (2005).
34. Blombach, B. & Seibold, G.M. Carbohydrate metabolism in *Corynebacterium glutamicum* and applications for the metabolic engineering of L-lysine production strains. *Appl Microbiol Biotechnol* **86**, 1313-1322 (2010).
35. Ikeda, M. Sugar transport systems in *Corynebacterium glutamicum*: features and applications to strain development. *Appl Microbiol Biotechnol* **96**, 1191-1200 (2012).
36. Dominguez, H. & Lindley, N.D. Complete sucrose metabolism requires fructose phosphotransferase activity in *Corynebacterium glutamicum* to ensure phosphorylation of liberated fructose. *Appl Environ Microbiol* **62**, 3878-3880 (1996).
37. Kiefer, P., Heinzle, E., Zelder, O. & Wittmann, C. Comparative metabolic flux analysis of lysine producing *Corynebacterium glutamicum* cultured on glucose or fructose. *Appl Environ Microbiol* **70**, 229-239 (2004).

38. Krings, E. *et al.* Characterization of myo-inositol utilization by *Corynebacterium glutamicum*: the stimulon, identification of transporters, and influence on L-lysine formation. *J Bacteriol* **188**, 8054-8061 (2006).
39. Ramp, P. *et al.* Physiological, biochemical, and structural bioinformatic analysis of the multiple inositol dehydrogenases from *Corynebacterium glutamicum*. *Microbiol Spectr* **10**, e01950-22 (2022).
40. Klaffl, S., Brocker, M., Kalinowski, J., Eikmanns, B.J. & Bott, M. Complex regulation of the phosphoenolpyruvate carboxykinase gene *pck* and characterization of its GntR-type regulator IolR as a repressor of *myo*-inositol utilization genes in *Corynebacterium glutamicum*. *J Bacteriol* **195**, 4283-4296 (2013).
41. Brüsseler, C. *et al.* The *myo*-inositol/proton symporter IolT1 contributes to D-xylose uptake in *Corynebacterium glutamicum*. *Bioresour Technol* **249**, 953-961 (2018).
42. Lindner, S.N., Seibold, G.M., Henrich, A., Krämer, R. & Wendisch, V.F. Phosphotransferase system-independent glucose utilization in *Corynebacterium glutamicum* by inositol permeases and glucokinases. *Appl Environ Microbiol* **77**, 3571-3581 (2011).
43. Bäumchen, C., Krings, E., Bringer, S., Eggeling, L. & Sahm, H. *Myo*-Inositol facilitator IolT1 and IolT2 enhance D-mannitol formation from D-fructose in *Corynebacterium glutamicum*. *FEMS Microbiol Lett* **290**, 227-235 (2009).
44. Ikeda, M. *et al.* Identification and application of a different glucose uptake system that functions as an alternative to the phosphotransferase system in *Corynebacterium glutamicum*. *Appl Microbiol Biotechnol* **90**, 1443-1451 (2011).
45. Moon, M.-W. *et al.* Analyses of enzyme II gene mutations for sugar transport and heterologous expression of fructokinase gene in *Corynebacterium glutamicum* ATCC 13032. *FEMS Microbiol Lett* **244**, 259-266 (2005).
46. Baumgart, M. *et al.* Construction of a prophage-free variant of *Corynebacterium glutamicum* ATCC 13032 for use as a platform strain for basic research and industrial biotechnology. *Appl Environ Microbiol* **79**, 6006-6015 (2013).
47. Meiswinkel, T.M., Gopinath, V., Lindner, S.N., Nampoothiri, M. & Wendisch, V.F. Accelerated pentose utilization by *Corynebacterium glutamicum* for accelerated production of lysine, glutamate, ornithine and putrescine. *Microb Biotechnol* **6**, 131-140 (2013).
48. Bakkes, P.J. *et al.* Improved pEKEx2-derived expression vector for tightly controlled production of recombinant proteins in *Corynebacterium glutamicum*. *Plasmid* **112**, 102540 (2020).
49. Xu, J.-Z., Ruan, H.-Z., Yu, H.-B., Liu, L.-M. & Zhang, W. Metabolic engineering of carbohydrate metabolism systems in *Corynebacterium glutamicum* for improving the efficiency of L-lysine production from mixed sugars. *Microb Cell Fact* **19**, 39 (2020).
50. Lindner, S.N., Knebel, S., Pallerla, S.R., Schoberth, S.M. & Wendisch, V.F. Cg2091 encodes a polyphosphate/ATP-dependent glucokinase of *Corynebacterium glutamicum*. *Appl Microbiol Biotechnol* **87**, 703-713 (2010).
51. Park, S.-Y., Kim, H.-K., Yoo, S.-K., Oh, T.-K. & Lee, J.-K. Characterization of *glk*, a gene coding for glucose kinase of *Corynebacterium glutamicum*. *FEMS Microbiol Lett* **188**, 209-215 (2000).
52. Monje-Galvan, V., Warburton, L. & Klauda, J.B. Setting up all-atom molecular dynamics simulations to study the interactions of peripheral membrane proteins with model lipid bilayers. *Methods Mol Biol* **1949**, 325-339 (2019).

53. Lomize, M.A., Pogozheva, I.D., Joo, H., Mosberg, H.I. & Lomize, A.L. OPM database and PPM web server: resources for positioning of proteins in membranes. *Nucleic Acids Res* **40**, D370-376 (2012).
54. Schymkowitz, J. *et al.* The FoldX web server: an online force field. *Nucleic Acids Res* **33**, W382-388 (2005).
55. Gentile, R. *et al.* Molecular mechanisms underlying medium-chain free fatty acid-regulated activity of the phospholipase PlaF from *Pseudomonas aeruginosa*. *JACS Au* **4**, 958-973 (2024).
56. Tokuriki, N., Stricher, F., Schymkowitz, J., Serrano, L. & Tawfik, D.S. The stability effects of protein mutations appear to be universally distributed. *J Mol Biol* **369**, 1318-1332 (2007).
57. Özcan, N. *et al.* Osmolality, temperature, and membrane lipid composition modulate the activity of betaine transporter BetP in *Corynebacterium glutamicum*. *J Bacteriol* **189**, 7485-7496 (2007).
58. Klatt, S. *et al.* Identification of novel lipid modifications and intermembrane dynamics in *Corynebacterium glutamicum* using high-resolution mass spectrometry. *J Lipid Res* **59**, 1190-1204 (2018).
59. Pfleger, C., Rathi, P.C., Klein, D.L., Radestock, S. & Gohlke, H. Constraint network analysis (CNA): a Python software package for efficiently linking biomacromolecular structure, flexibility, (thermo-)stability, and function. *J Chem Inf Model* **53**, 1007-1015 (2013).
60. Pfleger, C. *et al.* Ensemble- and rigidity theory-based perturbation approach to analyze dynamic allostery. *J Chem Theory Comput* **13**, 6343-6357 (2017).
61. Pfleger, C., Radestock, S., Schmidt, E. & Gohlke, H. Global and local indices for characterizing biomolecular flexibility and rigidity. *J Comput Chem* **34**, 220-233 (2013).
62. Pfleger, C. *et al.* Allosteric signaling in C-linker and cyclic nucleotide-binding domain of HCN2 channels. *Biophys J* **120**, 950-963 (2021).
63. Preising, M.N. *et al.* Biallelic mutation of human SLC6A6 encoding the taurine transporter TAUT is linked to early retinal degeneration. *FASEB J* **33**, 11507-11527 (2019).
64. Wifling, D. *et al.* Basal histamine H_4 receptor activation: Agonist mimicry by the diphenylalanine motif. *Chemistry* **25**, 14613-14624 (2019).
65. Drew, D., North, R.A., Nagarathinam, K. & Tanabe, M. Structures and general transport mechanisms by the Major Facilitator Superfamily (MFS). *Chem Rev* **121**, 5289-5335 (2021).
66. Pao, S.S., Paulsen, I.T. & Saier, M.H., Jr. Major facilitator superfamily. *Microbiol Mol Biol Rev* **62**, 1-34 (1998).
67. Acevedo-Rocha, C.G. *et al.* Pervasive cooperative mutational effects on multiple catalytic enzyme traits emerge via long-range conformational dynamics. *Nat Commun* **12**, 1621 (2021).
68. Klingenberg, M. Ligand-protein interaction in biomembrane carriers. The induced transition fit of transport catalysis. *Biochemistry* **44**, 8563-8570 (2005).
69. Bogdanov, M. & Dowhan, W. Phosphatidylethanolamine is required for *in-vivo* function of the membrane-associated lactose permease of *Escherichia coli*. *J. Biol. Chem.* **270**, 732-739 (1995).
70. Kaback, H.R. & Guan, L. It takes two to tango: The dance of the permease. *J Gen Physiol* **151**, 878-886 (2019).
71. Bivona, L., Zou, Z., Stutzman, N. & Sun, P.D. Influence of the second amino acid on recombinant protein expression. *Protein Expr Purif* **74**, 248-256 (2010).
72. Seo, S.W. *et al.* Predicitve design of mRNA translation initiation region to control prokaryotic translation efficiency. *Metab Eng* **15**, 67-74 (2013).

73. Chen, Y.-L. & Wen, J.-D. Translation initiation site of mRNA is selected through dynamic interaction with the ribosome. *Proc Natl Acad Sci USA* **119**, e2118099119 (2022).
74. Katano, H., Takakuwa, M., Itoh, T. & Hibi, T. Colorimetric determination of fructose for the high-throughput microtiter plate assay of glucose isomerase. *Biosci Biotech Biochem* **79**, 1057-1060 (2015).
75. Gonzalez de Valdivia, E.I. & Isaksson, L.A. A codon window in mRNA downstream of the initiation codon where NGG codons give strongly reduced gene expression in *Escherichia coli*. *Nucleic Acids Res* **32**, 5198-5205 (2004).
76. Gaikwad, S.M., Rao, M.B. & Deshpande, V.V. D-Glucose/xylose isomerase from *Streptomyces* - differential roles of magnesium and cobalt ions. *Enzyme Microb Technol.* **14**, 317-320 (1992).
77. Asensio, J.L., Ardá, A., Cañada, F.J. & Jiménez-Barbero, J. Carbohydrate-aromatic interactions. *Acc. Chem. Res.* **46**, 946-954 (2013).
78. Hudson, K.L. *et al.* Carbohydrate-aromatic interactions in proteins. *J. Am. Chem. Soc.* **137**, 15152-15160 (2015).
79. Kiessling, L.L. & Diehl, R.C. CH-π Interactions in glycan recognition. *ACS Cheml Biol* **16**, 1884-1893 (2021).
80. Kumari, M., Balaji, P.V. & Sunoj, R.B. Quantification of binding affinities of essential sugars with a tryptophan analogue and the ubiquitous role of C-H•••π interactions. *Phys. Chem. Chem. Phys.* **13**, 6517-6530 (2011).
81. Abramson, J. *et al.* Accurate structure prediction of biomolecular interactions with AlphaFold 3. *Nature* **630**, 493-500 (2024).
82. Uhde, A. *et al.* Transcription of sialic acid catabolism genes in *Corynebacterium glutamicum* is subject to catabolite repression and control by the transcriptional repressor NanR. *J Bacteriol* **198**, 2204-2218 (2016).
83. Walter, T. *et al.* Physiological response of *Corynebacterium glutamicum* to indole. *Microorganisms* **8**, 1945 (2020).
84. Frunzke, J., Engels, V., Hasenbein, S., Gätgens, C. & Bott, M. Co-ordinated regulation of gluconate catabolism and glucose uptake in *Corynebacterium glutamicum* by two functionally equivalent transcriptional regulators, GntR1 and GntR2. *Mol Microbiol* **67**, 305-322 (2008).
85. Kim, H.-J., Hyun, E.-K., Kim, Y.-S., Lee, Y.-J. & Oh, D.-K. Characterization of an *Agrobacterium tumefaciens* D-psicose 3-epimerase that converts D-fructose to D-psicose. *Appl Environ Microbiol* **72**, 981-985 (2006).
86. Yoshihara, A. *et al.* Purification and characterization of D-allulose 3-epimerase derived from *Arthrobacter globiformis* M30, a GRAS microorganism. *J Biosci Bioeng* **123**, 170-176 (2017).
87. Itoh, H. *et al.* Purification and characterization of D-tagatose 3-epimerase from *Pseudomonas* sp. ST-24. *Biosci Biotech Biochem* **58**, 2168-2171 (1994).
88. Chen, X. *et al.* Production of D-psicose from D-glucose by co-expression of D-psicose 3-epimerase and xylose isomerase. *Enzyme Microb Technol* **105**, 18-23 (2017).
89. Engels, V., Georgi, T. & Wendisch, V.F. ScrB (Cg2927) is a sucrose-6-phosphate hydrolase essential for sucrose utilization by *Corynebacterium glutamicum*. *FEMS Microbiol Lett* **289**, 80-89 (2008).
90. Chovancova, E. *et al.* CAVER 3.0: a tool for the analysis of transport pathways in dynamic protein structures. *PLoS Comput. Biol.* **8**, e1002708 (2012).

91. Hanahan, D. Studies on transformation of *Escherichia coli* with plasmids. *J Mol Biol* **166**, 557-580 (1983).
92. Kortmann, M., Kuhl, V., Klaffl, S. & Bott, M. A chromosomally encoded T7 RNA polymerase-dependent gene expression system for *Corynebacterium glutamicum*: construction and comparative evaluation at the single-cell level. *Microb Biotechnol* **8**, 253-265 (2015).
93. Schäfer, A. *et al.* Small mobilizable multi-purpose cloning vectors derived from the *Escherichia coli* plasmids pK18 and pK19: selection of defined deletions in the chromosome of *Corynebacterium glutamicum*. *Gene* **145**, 69-73 (1994).
94. Ramp, P. *et al.* Metabolic engineering of *Corynebacterium glutamicum* for production of *scyllo*-inositol, a drug candidate against Alzheimer's disease. *Metab Eng* **67**, 173-185 (2021).
95. Green, M.R. & Sambrook, J. Molecular cloning: a laboratory manual, 3rd ed. *Cold Spring Harb Lab. Press, Cold Spring Harbor, NY* (2012).
96. Gibson, D.G. *et al.* Enzymatic assembly of DNA molecules up to several hundred kilobases. *Nat Methods* **6**, 343-345 (2009).
97. van der Rest, M.E., Lange, C. & Molenaar, D. A heat shock following electroporation induces highly efficient transformation of *Corynebacterium glutamicum* with xenogeneic plasmid DNA. *Appl Microbiol Biotechnol* **52**, 541-545 (1999).
98. Kensy, F., Zang, E., Faulhammer, C., Tan, R.K. & Büchs, J. Validation of a high-throughput fermentation system based on online monitoring of biomass and fluorescence in continuously shaken microtiter plates. *Microb. Cell Fact.* **8**, 31 (2009).
99. Keilhauer, C., Eggeling, L. & Sahm, H. Isoleucine synthesis in *Corynebacterium glutamicum*: molecular analysis of the ilvB-ilvN-ilvC operon. *J Bacteriol* **175**, 5595-5603 (1993).
100. Bradford, M.M. A rapid and sensitive method for the quanitification of microgram quantities of protein utilizing the principle of protein-dye binding. *Anal Biochem* **72**, 248-254 (1976).
101. Mulnaes, D. *et al.* TopModel: Template-based protein structure prediction at low sequence identity using top-down consensus and deep neural networks. *J Chem Theory Comput* **16**, 1953-1967 (2020).
102. Berman, H.M. *et al.* The Protein Data Bank. *Nucleic Acids Res.* **28**, 235-242 (2000).
103. UniProt, C. UniProt: the Universal Protein Knowledgebase in 2023. *Nucleic Acids Res* **51**, D523-D531 (2023).
104. Mulnaes, D. & Gohlke, H. TopScore: Using deep neural networks and large diverse data sets for accurate protein model quality assessment. *J Chem Theory Comput* **14**, 6117-6126 (2018).
105. Guerois, R., Nielsen, J.E. & Serrano, L. Predicting changes in the stability of proteins and protein complexes: a study of more than 1000 mutations. *J Mol Biol* **320**, 369-387 (2002).
106. Benardout, M., Le Gresley, A., ElShaer, A. & Wren, S.P. Fructose malabsorption: causes, diagnosis and treatment. *Brit. J. Nutr.* **127**, 481-489 (2022).
107. OEDocking, O. OEDocking 4.3.0.3. Vol. version 4.3.0.3. http://www.eyesopen.com (Cadence Molecular Sciences, Inc., Santa Fe, NM).
108. OpenEye. OMEGA Vol. 4.1.1.1 http://www.eyesopen.com (OpenEye Scientific Software,, Santa Fe, NM, USA, 2019).
109. Morris, G.M. *et al.* Automated docking using a Lamarckian genetic algorithm and an empirical binding free energy function. *J Comput Chem* **19**, 1639-1662 (1999).
110. Dittrich, J., Schmidt, D., Pfleger, C. & Gohlke, H. Converging a knowledge-based scoring function: DrugScore^{2018} *J Chem Inf Model* **59**, 509-521 (2019).

111. Oliva, L., Fernandez-Lopez, J.A., Remesar, X. & Alemany, M. The anomeric nature of glucose and its implications on its analyses and the influence of diet: Are routine glycaemia measurements reliable enough? *J. Endocrinol. Metab.* **9**, 63-70 (2019).
112. Deng, D. *et al.* Molecular basis of ligand recognition and transport by glucose transporters. *Nature* **526**, 391-6 (2015).
113. Frisch, M.J. *et al.* Gaussian 16 Rev. C.01. (Wallingford, CT, 2016).
114. Bayly, C.I., Cieplak, P., Cornell, W.D. & Kollman, P.A. A well-behaved eectrostatic potential based method using charge restraints for deriving atomic charges - the RESP model. *J. Phys. Chem.* **97**, 10269-10280 (1993).
115. Cornell, W.D. *et al.* A second generation force field for the simulation of proteins, nucleic acids, and organic molecules *J. Am. Chem. Soc.* **118**, 2309-2309 (1996).
116. Greenwood, J.R., Calkins, D., Sullivan, A.P. & Shelley, J.C. Towards the comprehensive, rapid, and accurate prediction of the favorable tautomeric states of drug-like molecules in aqueous solution. *J Comput Aided Mol Des* **24**, 591-604 (2010).
117. Johnston, R.C. *et al.* Epik: pK_a and protonation state prediction through machine learning. *J Chem Theory Comput* **19**, 2380-2388 (2023).
118. Shelley, J.C. *et al.* Epik: a software program for pK_a prediction and protonation state generation for drug-like molecules. *J Comput Aided Mol Des* **21**, 681-691 (2007).
119. Schrödinger. Maestro. (Schrödinger LLC, New York, NY, 2023).
120. Martinez, L., Andrade, R., Birgin, E.G. & Martinez, J.M. PACKMOL: a package for building initial configurations for molecular dynamics simulations. *J Comput Chem* **30**, 2157-2164 (2009).
121. Schott-Verdugo, S. & Gohlke, H. PACKMOL-Memgen: A simple-to-use, generalized workflow for membrane-protein-lipid-bilayer system building. *J Chem Inf Model* **59**, 2522-2528 (2019).
122. Qian, W. *et al.* Comparative and functional genomic analyses of the pathogenicity of phytopathogen *Xanthomonas campestris* pv. *campestris*. *Genome Res* **15**, 757-767 (2005).
123. Munshi, P. *et al.* Neutron structure of the cyclic glucose-bound xylose isomerase E186Q mutant. *Acta Crystallogr D Struct Biol.* **70**, 414-420 (2014).
124. Whitlow, M. *et al.* A metal-mediated hydride shift mechanism for xylose isomerase based on the 1.6 A *Streptomyces rubiginosus* structures with xylitol and D-xylose. *Proteins* **9**, 153-173 (1991).
125. Cao, Y. *et al.* Crystal structure of a phosphorylation-coupled saccharide transporter. *Nature* **473**, 50-54 (2011).
126. Case, D.A. *et al.* AmberTools. *J Chem Inf Model* **63**, 6183-6191 (2023).
127. Tian, C. *et al.* ff19SB: Amino-acid-specific protein backbone parameters trained against quantum mechanics energy surfaces in solution. *J Chem Theory Comput* **16**, 528-552 (2020).
128. Dickson, C.J., Walker, R.C. & Gould, I.R. Lipid21: Complex lipid membrane smulations with AMBER. *J. Chem. Theory Comput.* **18**, 1726-1736 (2022).
129. Kirschner, K.N. *et al.* GLYCAM06: a generalizable biomolecular force field. Carbohydrates. *J Comput Chem* **29**, 622-655 (2008).
130. Xiong, Y., Izadi, S. & Onufriev, A.V. Fast polarizable water model for atomistic simulations. *J Chem Theory Comput* **18**, 6324-6333 (2022).
131. Xiong, Y., Izadi, S. & Onufriev, A.V. Correction to "Fast polarizable water model for atomistic simulations". *J Chem Theory Comput* **19**, 377 (2023).
132. Li, P., Song, L.F. & Merz, K.M., Jr. Systematic parameterization of monovalent ions employing the nonbonded model. *J Chem Theory Comput* **11**, 1645-1657 (2015).

133. Sengupta, A., Li, Z., Song, L.F., Li, P. & Merz, K.M., Jr. Correction to "Parameterization of monovalent ions for the OPC3, OPC, TIP3P-FB, and TIP4P-FB water models". *J Chem Inf Model* **61**, 3734-3735 (2021).
134. Sengupta, A., Li, Z., Song, L.F., Li, P. & Merz, K.M., Jr. Parameterization of monovalent ions for the OPC3, OPC, TIP3P-FB, and TIP4P-FB water models. *J Chem Inf Model* **61**, 869-880 (2021).
135. Kräutler, V., Van Gunsteren, W.F. & Hünenberger, P.H. A fast SHAKE:: Algorithm to solve distance constraint equations for small molecules in molecular dynamics simulations. *J Comput Chem* **22**, 501-508 (2001).
136. Hopkins, C.W., Le Grand, S., Walker, R.C. & Roitberg, A.E. Long-time-step molecular dynamics through hydrogen mass repartitioning. *J Chem Theory Comput* **11**, 1864-1874 (2015).
137. Le Grand, S., Götz, A.W. & Walker, R.C. SPFP: Speed without compromise-A mixed precision model for GPU accelerated molecular dynamics simulations. *Comput Phys Commun* **184**, 374-380 (2013).
138. Quigley, D. & Probert, M.I. Langevin dynamics in constant pressure extended systems. *J Chem Phys* **120**, 11432-11441 (2004).
139. Berendsen, H.J.C., Postma, J.P.M., Vangunsteren, W.F., Dinola, A. & Haak, J.R. Molecular-dynamics with coupling to an external Bath. *J. Chem. Phys.* **81**, 3684-3690 (1984).
140. Lin, Y., Pan, D., Li, J., Zhang, L. & Shao, X. Application of Berendsen barostat in dissipative particle dynamics for nonequilibrium dynamic simulation. *J Chem Phys* **146**, 124108 (2017).
141. Hermans, S.M.A., Pfleger, C., Nutschel, C., Hanke, C.A. & Gohlke, H. Rigidity theory for biomolecules: concepts, software, and applications. *WIREs Comput Mol Sci* **7**, e1311 (2017).
142. Jacobs, D.J., Rader, A.J., Kuhn, L.A. & Thorpe, M.F. Protein flexibility predictions using graph theory. *Proteins* **44**, 150-165 (2001).
143. Dahiyat, B.I., Gordon, D.B. & Mayo, S.L. Automated design of the surface positions of protein helices. *Protein Sci.* **6**, 1333-1337 (1997).
144. Becker, D., Bharatam, P.V. & Gohlke, H. F/G region rigidity is inversely correlated to substrate promiscuity of human CYP isoforms involved in metabolism. *J. Chem. Inf. Model.* **61**, 4023-4030 (2021).
145. Miller, B.R. *et al.* MMPBSA.py: An efficient program for end-state free energy calculations. *J. Chem. Theory Comput.* **8**, 3314-3321 (2012).